Cell-type-specific genomics reveals histone modification dynamics in mammalian meiosis

Authors

Kwan-Wood Gabriel Lam, Kevin Brick, Gang Cheng, Florencia Pratto and R. Daniel Camerini-Otero*

Affiliations

Genetics and Biochemistry Branch, National Institute of Diabetes, Digestive and Kidney Diseases, National Institutes of Health, Bethesda, MD, USA

*Corresponding author

Abstract

Meiosis is the specialized cell division during which parental genomes recombine to create genotypically unique gametes. Despite its importance, mammalian meiosis cannot be studied *in vitro,* greatly limiting mechanistic studies*. In vivo,* meiocytes progress asynchronously through meiosis and therefore the study of specific stages of meiosis is a challenge. Here, we describe a simple method for isolating pure sub-populations of meiocytes that allows for detailed study of meiotic sub-stages. Interrogating the H3K4me3 landscape revealed dynamic chromatin transitions between sub-stages of meiotic prophase I, both at sites of genetic recombination and at gene promoters. We also leveraged this method to perform the first comprehensive, genome-wide survey of histone marks in meiotic prophase, revealing a heretofore unappreciated complexity of the epigenetic landscape at meiotic recombination hotspots. Ultimately, this study presents a simple, scalable framework for interrogating the complexities of mammalian meiosis.

Main

Meiosis is the specialized cell division required to form gametes. Despite its importance, many of the molecular mechanisms of meiosis remain poorly studied in higher eukaryotes. This is largely because mammalian meiosis cannot be adequately recapitulated *in vitro*[1]. *In vivo*, meiosis either occurs in a difficult-to-isolate niche, such as the fetal ovary, or in an asynchronously dividing tissue such as in adult testis. As a result, technical challenges preclude the isolation and study of specific meiotic sub-stages. Here, we introduce a method to isolate and purify stage-specific meiotic nuclei. We leveraged this method to interrogate the histone modification landscape in meiotic prophase I (MPI) in unprecedented detail.

Extant methods to study sub-stages of meiotic prophase have been dominated by the use of crude enrichment strategies. One common approach has been to study spermatocytes in juvenile mice, where the first wave of meiosis progresses relatively synchronously[2,3]. Nonetheless, most cells in juvenile testis are not at the stage of interest because this synchrony is not absolute, and there are many non-meiotic cells. Furthermore, differences between the first and the subsequent rounds of spermatogenesis[4,5] may preclude generalization to adults. Chemically induced synchronization of meiosis has recently been developed[6], however the application is technically cumbersome and the consequences of chemical treatment have not been explored. An alternative to enrichment is the isolation of meiotic sub-stages. Fluorescence-activated cell sorting (FACS) or sedimentation based methods have been used to isolate particular sub-stages[7–9]. However, since these methods rely on imprecise metrics such as cell size and chromatin content, the isolation and distinction between many sub-stages is challenging. Thus, isolation-based approaches have not been broadly adapted to the study of the dynamic molecular events during meiosis.

We have devised a simple, yet highly specific strategy to isolate pure sub-populations of meiotic nuclei. This approach uses a variant of FACS[10] in which antibodies to intra-nuclear markers are used to select nuclei of interest. The proteins present in different meiotic sub-stages are well studied[11–14] and we leverage this knowledge to isolate nuclei in which specific combinations of proteins are expressed. This allowed for the isolation of meiotic sub-populations ranging from 74-96% purity. Nuclei are fixed before sorting, which preserves *in vivo* interactions and prevents degradation during sample processing. Importantly, this fixation also means our method is the first to allow for downstream interrogation of genome-wide protein-DNA interactions in meiotic sub-stages.

Although comprehensively studied in somatic cells, little is known about histone modification dynamics in meiotic cells. A case in point are the histone modifications that precede meiotic DSB formation, an early event in meiotic recombination. Programmed DNA double-strand breaks (DSBs) are targeted to sites defined by DNA binding and subsequent H3K4/K36-trimethylation by the PRDM9 protein[15,16]. PRDM9 gene expression[17], nuclear protein levels of PRDM9[18] and microscopy-based estimates of DSB formation[19,20] all imply that PRDM9 marks sites for DSB formation at the onset of MPI. Using chromatin immunoprecipitation followed by high throughput sequencing (ChIP-Seq) on sorted populations of nuclei, we determined that Histone H3 Lysine 4 trimethylation (H3K4me3) varies from stage-to-stage at meiotic DSB hotspots, gene promoters and a vast number of heretofore unannotated sites likely to be functional elements, such as enhancers and cryptic promoters. These are the first genome-wide analyses of the dynamic chromatin landscape in meiosis. Studies of individual DSB hotspots have implied that H3K4/K36me3 alone do not fully describe the chromatin landscape at these sites[21]. Indeed, we found that the histone code at DSB hotspots is more complex than has been previously appreciated, with multiple histone tail modifications exhibiting enrichment. This includes histone acetylation marks unlikely to have been deposited by the DSB-defining histone methyltransferase PRDM9.

Together, these data demonstrate the simplicity, utility and feasibility of our approach. This method opens the door to a far better understanding of the molecular mechanisms underlying meiosis and other complex developmental processes.

Results

Isolation of stage-specific spermatocyte nuclei

We first devised a discriminative panel of intra-nuclear proteins to distinguish between five, classically-defined MPI sub-stages; leptonema, zygonema, early pachynema, late pachynema and diplonema (Fig. 1). Nuclei were extracted from formaldehyde-fixed testes from adult male mice, then incubated with antibodies against the desired proteins (see methods). Nuclei were also stained with DAPI to allow measurement of DNA content. The combinatorial signals from these fluorescent markers were subsequently used to isolate specific sub-populations of spermatocyte nuclei using FACS (Fig. 2A and B; see methods).

We used the meiosis-specific protein SCP3 to distinguish post-replicative meiotic prophase nuclei (4C) from fully replicated mitotic nuclei (also 4C). We then combined SCP3 with other markers for FACS. Our combination of antibodies required two separate sorts; one to isolate leptotene nuclei and a second to isolate the other four sub-stages (Fig. 2A and B). In male mice, STRA8 regulates the entry to meiotic S phase, and is expressed from primitive spermatogonia to leptotene spermatocytes[14]. We therefore used STRA8 to isolate leptotene nuclei from later stages. To isolate the four other meiotic stages, we used the presence or absence of H1t and quantitative differences in SCP1 intensity (Fig. 1, Fig. 2A). H1t (testis-specific histone H1) is present from mid pachynema through MPI[22], whereas SCP1 is a marker of progressive chromosome synapsis from zygotene to pachytene stage and the SCP1 signal is diminished in diplonema when chromosomes desynapse[12] (Fig. 1). Thus, we collected seven populations, assessed the purity of each population and determined the gating thresholds for the four meiotic sub-stages (Fig. 2B and C).

The purity of each sorted population was assessed using immunofluorescence microscopy to stage the nuclei according to the known localization of markers (Fig. 1, Fig. 2A and C, Supplementary Fig. 1, see methods)[11–14]. The purity of the sorted leptotene population was 94.6% - 97.9% (n = 2), a >20-fold increase in purity compared to the percentage of leptotene cells in whole testis (4.1% - 5.5% (n = 2), Fig. 2C). The purity of the other four populations ranged from 73.9 - 90.4%, each more than 10-fold enriched relative to the starting population from whole testis (Fig. 2C). The least pure sample was that of zygotene (71.3% - 78.7% (n = 3)), likely because we rely entirely on quantitative differences in SCP1 to distinguish between adjacent stages (Fig. 1, Fig. 2B and C). Narrowing of the gate can increase purity but at the cost of yield (data not shown). Quantitative thresholding issues also explain the 9.0% - 16.9% (n = 3) of zygotene nuclei found in the sorted early pachytene population (Fig. 1, Fig. 2B and C).

From a single adult mouse, we obtained between 115,000 and 400,000 nuclei for each meiotic sub-stage (Fig. 2D). This range broadly reflects differences in the proportion of each sub-stage in the adult testis, where leptotene and zygotene nuclei are less abundant. Thus, the different sub-stages are isolated in sufficient numbers for experiments using standard genomics protocols[23].

Stage-specific ChIP-Seq reveals histone modification dynamics in meiosis

We next used ChIP-Seq to examine the dynamics of H3K4me3 in MPI. H3K4me3 is of key biological interest in meiosis because it regulates multiple independent dynamic processes during MPI; H3K4me3 is found at gene promoters and its presence correlates with active transcription[24,25], whereas

PRDM9-mediated H3K4me3 marks the future sites of meiotic DSBs genome-wide[26,27]. We therefore performed H3K4me3 ChIP-Seq in the five aforementioned sorted populations to assess the temporal dynamics of this histone mark in MPI.

To establish the requirements for the amount of chromatin needed for ChIP-Seq, we examined the ChIP-Seq quality of samples using different amounts of starting nuclei (5,000–264,000). Between 7,517 and 47,804 H3K4me3 peaks were detected in each sub-stage (Table 1). We merged these peaks to yield a super-set of 58,862 H3K4me3 peaks present in at least one sub-stage. The Signal Percentage of Tags (SPoT; a measure of the signal-to-noise ratio of ChIP-Seq samples[28]), ranged from 13% to 50%, far exceeding ENCODE recommendations of > 1%[29]. As expected, samples derived from fewer nuclei had a lower SPoT and detected fewer H3K4me3 peaks (Table 1). Importantly, approximately 40,000–60,000 nuclei are sufficient to begin reaching saturation levels of peak detection (Fig. 3A). Thus, sorted populations of meiotic nuclei are amenable to ChIP-Seq with little, if any loss of sample quality.

To allow for quantitative cross-comparison of H3K4me3 signals from samples of differing quality, we first normalized H3K4me3 peak strength in each sample by the signal at 99 gene promoters at which the H3K4me3 signal was relatively invariant across MPI (<1.2-fold change in all pairwise comparisons between stages, see methods for details). We observed a highly dynamic H3K4me3 signal at hotspots in MPI (Fig. 3B and C); the H3K4me3 signal first appears at leptonema, and is maximal at zygonema, decreases in early pachynema and is gone by late pachynema (Fig. 3C). The maximal signal at zygonema was somewhat surprising because DSBs are formed and nuclear PRDM9 protein levels are maximal at leptonema[18].

Intriguingly, at hotspots that are used more frequently for DSB formation, H3K4me3 is relatively weak at zygonema compared to leptonema

(Supplementary Fig. 2A and B). This implies that DSB formation or repair removes H3K4me3-modified nucleosomes, similar to findings in *Saccharomyces cerevisae*[30]. PRDM9-mediated H3K4me3 decreases after zygonema, however, the bias toward strong hotspots is not observed (Supplementary Fig. 2C). This indicates that the H3K4me3 reduction may be caused by mechanisms other than nucleosome eviction resulting from DSB formation or repair. Instead, PRDM9 may mark more sites than are used for DSB formation, and the decrease from zygonema to early pachynema reflects systematic removal of excess marks. This conclusion is reinforced by the strong H3K4me3 signal at early pachynema, when DSB formation is unlikely[31,32].

The H3K4me3 level at gene promoters is correlated with gene expression in mitotic cells[25]. We therefore investigated if the temporal dynamics of H3K4me3 at transcription start sites (TSSs) is predictive of meiotic gene expression patterns.

Stage-specific gene expression in MPI has been deduced from classical cell sorting of meiotic cells followed by RNA-Seq[9,33]. We found that the H3K4me3 profiles at TSSs were positively correlated with gene expression through MPI (Fig. 3D, $R = 0.32$; Spearman test). This correlation was highly significant, far higher than the maximum correlation observed in randomized comparisons (empirical $P < 0.0001$; $N = 10{,}000$ bootstraps, $R_{max} = 0.03$, see methods). To explore the relationship between H3K4me3 and gene expression in more detail, we clustered transcripts based on the temporal H3K4me3 pattern (Fig. 3D; optimal clusters = 3; k-means clustering using gap statistic[34]). There was significant correlation with gene expression in all clusters ($P < 0.0001$; $N = 10{,}000$ bootstraps, range; $0.14 \leq R \leq 0.43$) (Fig. 3D). Each cluster is composed of a large fraction of transcripts where H3K4me3 and gene expression correlate very well. Nonetheless, there are also many transcripts that exhibit non-correlated H3K4me3 and expression. This is particularly evident in cluster 1, where many genes have higher mRNA levels late in MPI than we would predict from H3K4me3 data (Supplementary Fig. 3). This may be explained by mRNA accumulation through MPI, or by H3K4me3 marking poised, but not yet active promoters[35]. Genes in cluster 3 are predictably less affected by these confounding effects and the correlation is far higher for this cluster. Together, these data demonstrate that ChIP-Seq of H3K4me3 in stage-specific nuclei reveals a dynamic that parallels that of gene expression. These data also reveal an intricate and poorly understood interplay between H3K4me3 and gene expression during MPI.

H3K4me3 dynamics at other genomic elements

Dynamic H3K4-trimethylation is observed at both gene promoters and DSB hotspots in MPI. However, almost half of the H3K4me3 peaks detected (28,951/59,191) are outside of these sites (Supplementary Fig. 4A). These unannotated H3K4me3 peaks may represent enhancers, cryptic promoters or other functional elements. To assess the H3K4me3 dynamics of these peaks, we derived an MPI profile for each H3K4me3 peak across the five MPI stages, then performed unbiased k-means clustering. This approach was validated by the presence of a large cluster that peaks at zygonema and that mostly contains PRDM9-defined DSB hotspots (cluster 2; Supplementary Fig. 4B-D; 92% of hotspots occur in this cluster). A subset of unannotated peaks (17%) also occur in this cluster (cluster 2; Supplementary Fig. 4D) and may represent sites of PRDM9 binding that were not detected in hotspot mapping experiments. Alternatively, we cannot rule out that a cluster of cryptic functional sites simply exhibit a similar dynamic. The remaining unannotated H3K4me3 peaks exhibit an MPI dynamic that broadly mirrors that of H3K4me3 at TSS (Supplementary Fig. 4B, D). It seems likely therefore that functional elements at these sites play a role in regulating meiotic progression. These dynamic, but unannotated sites represent a completely unexplored aspect of the regulation of mammalian meiosis.

Clustering also allowed us to study H3K4me3 dynamics at sites involved in other important processes during MPI. In particular, we examined H3K4me3 sites that are used for DSB targeting in mice that lack functional PRDM9[26,27]. H3K4me3 peaks used as “default” hotspot locations were predominantly those with peak signal in early MPI (Supplementary Fig. 4E).

Identifying other histone marks at hotspots

At DSB hotspots defined by PRDM9, H3K4me3 is necessary for DSB formation[36]. Nonetheless, H3K4me3 alone is not sufficient to define DSB sites, as this histone mark is also present at other functional sites, such as gene promoters. In mice, H3K36me3 is the only other histone mark described genome-wide at DSB hotspots[15], while other histone marks may also be involved in defining DSB sites[21,37,38]. The H3K36me3 ChIP-Seq signal at hotspots was weak compared to H3K4me3 ChIP-Seq [15], thus, having the correct population to interrogate appears important when exploring histone marks at hotspots. We therefore used our method to isolate target nuclei from adult mice for a systematic survey of multiple histone modifications.

We performed ChIP-Seq using 17 antibodies against histone methylation and acetylation marks on isolated nuclei (Fig. 4A and B). These marks were either previously analyzed at individual hotspots in mice[21,38] or reported to be enriched at DSB sites in other organisms[39,40]. In this exploratory phase, we did not perform ChIP-Seq in all five sub-populations, but instead, collected the SCP3+ and H1t– population (leptonema to early pachynema) in which the H3K4me3 signal at hotspots was apparent. As a positive control, H3K4me3 ChIP-Seq yielded a comparable SPoT (3% at hotspots) to that in the stage-specific experiments (Table 1).

H4K8ac, H4K12ac, H4K20me3, H3K4ac, H3K79me1, H3K79me3, H3K27me1, H3K9me2, H3K9me3 and H3K27me3 were not enriched at hotspots relative to controls (Fig. 4A, B; Supplementary Fig. 5). Most of these experiments showed enrichment at other functional genomic regions (Supplementary Fig. 6), lending confidence that lack of enrichment at hotspots is not the result of inefficient ChIP. Several experiments (H3K9me2, H3K27me1 and H3K79me1) did not show enrichment at other functional sites in the genome, therefore the lack of hotspot signal may simply result from poor ChIP-quality.

H3K4me1, H3K27ac and H4ac5 showed marginal enrichment at hotspots (Fig. 4A, B; Supplementary Fig. 5). The weak signals at hotspots are unlikely the result of sub-optimal ChIP-quality, as strong signals are seen at gene promoters and enhancers (Supplementary Fig. 6). Instead, these marks may be rapidly turned-over or present only in a sub-population of early spermatocytes. Indeed, a weak DSB-dependent H4ac5 signal was previously reported at two mouse hotspots[21].

PRDM9 can trimethylate both H3K4 and H3K36[36] and as expected, H3K4me3 and H3K36me3 were both enriched at hotspots (Fig. 4A and B; Supplementary Fig. 5). H3K4me2 and H3K9ac were also strongly enriched at DSB hotspots genome-wide; this clearly resolves the ambiguity from previous studies where these marks were only enriched at one individual hotspot[21]. H3K4me2 may be an intermediate of PRDM9 H3K4-trimethylation, however since PRDM9 lacks a histone acetyltransferase domain, it is unlikely that PRDM9 directly acetylates H3K9. In stage-specific experiments, the dynamics of H3K9ac through MPI resemble those of H3K4me3; signal is first observed at hotspots in leptonema, maximal at zygonema and progressively diminishes through diplonema (Fig. 4C). Thus, H3K9ac is a *bona-fide* marker of meiotic DSB hotspots genome-wide, explicitly demonstrating for the first time that proteins other than PRDM9 modify nucleosomes at the sites of DSB hotspots.

H3K4me3 is positively correlated with DSB frequency[27,41], but most variation in hotspot strength is not accounted for by changes in H3K4me3 (Spearman R^2 = 0.48) (Supplementary Fig. 7A). H3K36me3 was previously reported to slightly improve the correlation between H3K4me3 and DSB strength[42], therefore we tried to better predict hotspot strength using a combination of histone marks that are enriched at DSB hotspots. Multiple linear regression with all histone marks only slightly improved the correlation with hotspot strength (max R^2 = 0.51; Supplementary Fig. 7B; see methods) suggesting that these extra histone marks (including H3K36me3) do not offer an independent readout of DSB usage as compared to H3K4me3.

A histone code distinguishes DSB hotspots from PRDM9-independent H3K4me3 sites

In the absence of PRDM9, DSB hotspots occur at sites of non-PRDM9-mediated H3K4me3[27]. Nonetheless, in *wild-type* mice, PRDM9-defined H3K4me3 sites are used. In agreement with previous results[15,16], we found that H3K36me3 is a potent discriminator between DSB hotspots and other H3K4me3-marked sites in the genome (Fig. 4D). Among the other histones, H3K4me2 and H3K9ac can best distinguish hotspots (Fig. 4D; Supplementary Fig. 8). We excluded histone marks made by PRDM9 (H3K4me3 and H3K36me3), then performed principal component analysis to explore if any combination(s) of histone marks better define DSB hotspots. The most discriminative PC (PC3) captured signal from H3K4me1, H3K4me2 and H3K9ac (Fig. 4E), all marks that are enriched at DSB hotspots, however it did not discriminate hotspots any better than H3K4me2 alone. These data suggest that H3K36me3, H3K4me2, H3K9ac and to a lesser extent, H3K4me1, distinguish the chromatin at sites of PRDM9-marked DSB hotspots from that at other functional sites where H3K4 is tri-methylated.

Discussion

In this study, we developed a method to isolate highly pure populations of meiotic nuclei from whole testis. This method is simple, rapid, requires very little starting material, and resolves a major hurdle to studying meiosis in mammals. We have demonstrated that we can efficiently sort five populations of MPI nuclei, however, in principle, nuclei at any specific stage can be purified if the requisite antibodies are available. We obtained populations of up to 96% purity for a given meiotic sub-stage, negating the need to artificially synchronize meiosis using chemicals or the need to use juvenile mice to obtain enriched populations of meiocytes. This opens the door to many detailed studies of meiosis and also to experiments in challenging-to-breed knockout mice and importantly in humans, where other synchronization strategies are impractical.

Importantly, fixation prior to sorting allows for genome-wide interrogation of transient protein-DNA interactions in sorted populations. To this end, we profiled H3K4me3 using ChIP-Seq in five MPI populations, capturing extensive dynamics of this histone mark. The H3K4me3 marks made at DSB hotspots by PRDM9 appear in leptonema, are maximal in zygonema, then reduce in early pachynema before being removed by late pachynema. Intriguingly, the presence of robust H3K4me3 signal at early pachynema implies that PRDM9 trimethylates more nucleosomes than are used during DSB formation. An alternate explanation would require DSB formation in early pachynema. This is unlikely because homolog synapsis shuts down the DSB machinery in yeast[43] and an analogous system appears to operate in mammals[31,44]. These are the first data to demonstrate excess H3K4me3 by PRDM9 in *wild-type* mice, however recent work in mice co-expressing both endogenous and transgenic PRDM9 reached a similar conclusion[36].

H3K4me3 at gene promoters is also dynamic through MPI. By comparing H3K4me3 at promoters with gene expression, we found that while most transcript levels are predicted by H3K4me3, a large subset of transcripts exhibit gene expression that appears decoupled from H3K4me3 levels. Most such transcripts exhibit a strong H3K4me3 signal at the TSS in early MPI, but expression is maximal late in MPI; this may result from long-lived mRNA, from mRNA accumulation, or from H3K4me3 marks at the sites of poised RNA polymerase[35]. Indeed, these transcripts are intriguing candidates for further understanding gene regulation in MPI. Finally, whereas DSB hotspots and gene promoters constitute about half of the dynamic H3K4me3 marks in MPI, the functions of the other half of dynamic histone marks remain completely unknown. At least some of these sites are likely enhancers, and together, they represent a large, heretofore unstudied set of functional sites that may be modulating mouse meiosis.

To examine the chromatin landscape at DSB hotspots, we also performed the first systematic genome-wide survey on a wide repertoire of histone marks. Our ability to efficiently sort early MPI nuclei eliminated the need to perform these experiments in juvenile mice in which early MPI nuclei were only relatively enriched[15,45]. Aside from H3K4me3[27] and H3K36me3[15,16], H3K9ac, H3K4me2, H3K4me1, H3K27ac and H4ac5 were enriched at DSB hotspots genome-wide. Incorporating the extra information about these histone marks only marginally increases our ability to predict hotspot strength, implying that even the expanded chromatin landscape at hotspots remains a poor predictor of DSB formation. The genome is replete with H3K4me3 marks that are used for DSB formation in the absence of PRDM9, however, enigmatically, these sites are not used if PRDM9 is functional. We demonstrated that both H3K36me3[15,40,42], and multiple histone marks distinguish between these sites. Although this unique histone "code" may help the DSB machinery to distinguish PRDM9-defined H3K4me3 from other H3K4me3 marks, it is equally possible that direct interactions mediated by PRDM9 itself are important for this distinction. It seems unlikely that PRDM9 is responsible for all of the histone tail modifications at hotspots, therefore other histone remodelers are likely acting at the sites of PRDM9-marked H3K4/K36me3. H3K9ac and H3K4me3 are strength correlated, have a similar temporal dynamic and are of a similar magnitude, implying that they occur at a comparable frequency at hotspots. In mitotic cells, H3K9 acetylation is actively promoted at H3K4 trimethylated nucleosomes[46]. It is therefore likely that H3K9ac is a constitutive response to H3K4 trimethylation. Nonetheless, histone acetylation may be functionally important *per se* in the context of DSB formation;

for example, in fission yeast, H3K9 to H3A9 mutation eliminates H3K9ac and consequently reduces DSB formation[40].

Overall, we demonstrated that our simple, robust method can explore previously hidden dynamics of mammalian meiotic recombination. Importantly, our method is widely applicable to other organisms, tissues and cell types, paving the way for further understanding of the temporal dynamics of other developmental processes.

Data availability

The sequencing data reported in this paper are archived at the Gene Expression Omnibus (www.ncbi.nlm.nih.gov/geo) as accession no. GSE121760.

Acknowledgements

We thank members from Camerini-Otero's lab for discussions, and Galina Petukhova for insightful comments. We are grateful to Mary Ann Handel for sharing H1t antibodies. This study used the high performance computational capabilities of the Biowulf Linux cluster at the National Institutes of Health, Bethesda, MD (http://biowulf.nih.gov). We thank members from the NHLBI Flow Cytometry Core for assistance with nuclei sorting, and members from the NIDDK Genomics Core for assistance with high-throughput sequencing. This work was funded by the NIDDK Intramural Research Program (R.D.C.O).

Author contributions

K-W.G.L., K.B., F.P. and R.D.C-O. conceived the study and designed the experiments. K-W.G.L. and G.C. performed the experiments. K-W.G.L., K.B. and F.P. analyzed the data. K-W.G.L., K.B., F.P. and R.D.C-O. wrote the manuscript.

Table 1. Summary of cell-type-specific H3K4me3 ChIP-Seq.

Sub-stage	Replicate	DNA input (ng)	Nuclei (#)	SPoT (HS) (%)	SPoT (All) (%)	Peaks (#)
Leptonema	1	81	7,000	2	32	29,004
	2	1,306	109,000	4	45	47,804
Zygonema	1	342	28,000	2	15	12,367
	2	3,174	264,000	4	28	35,014
Early Pachynema	1	339	28,000	2	13	7,517
	2	1,693	141,000	4	34	36,125
Late Pachynema	1	126	10,000	1	23	11,577
	2	1,067	89,000	2	49	31,630
Diplonema	1	60	5,000	1	28	16,526
	2	1,196	100,000	2	50	25,605

Fig. 1

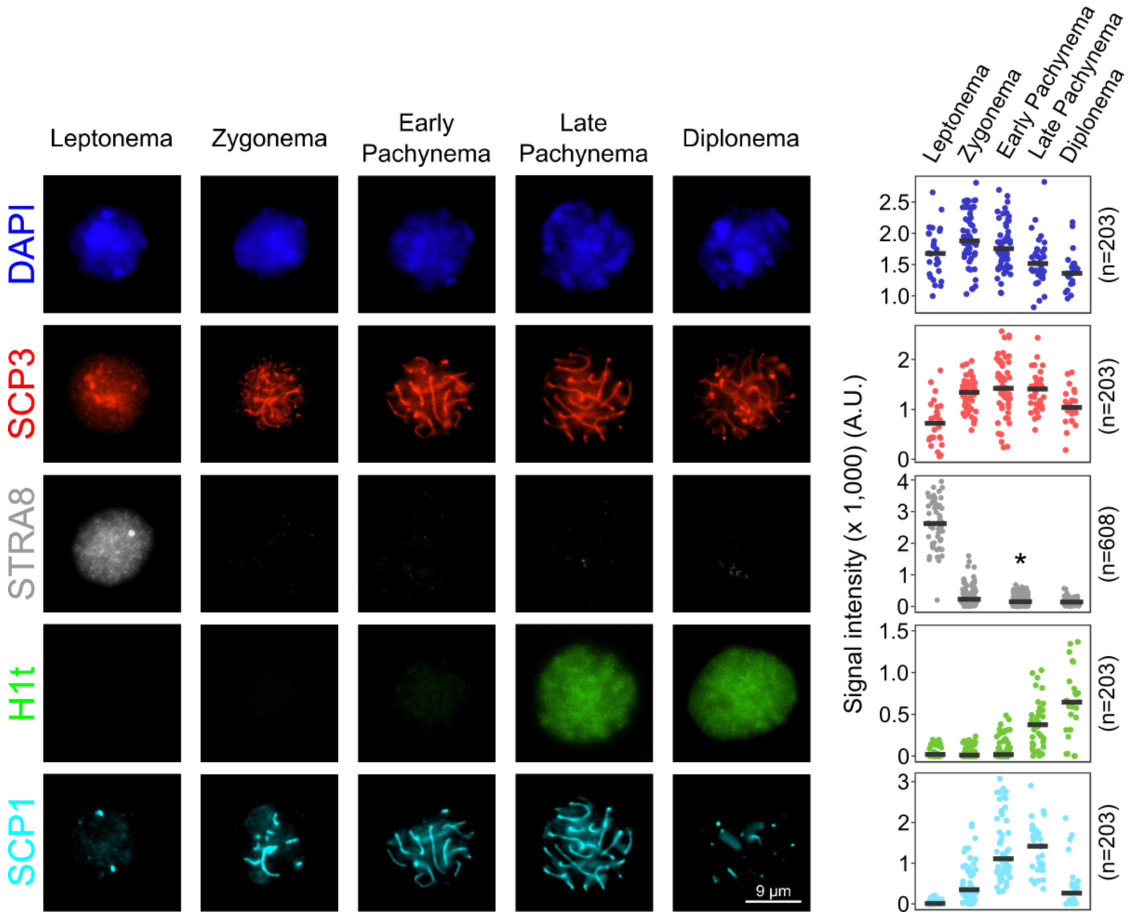

Fig 1: Immunofluorescence staining of spermatocyte nuclei.

Immunofluorescence images and signal quantification of stage-specific spermatocyte nuclei through meiosis prophase I. Details for signal quantification are described in Methods. Microscopic images are selected from two independent experiments in which two different combinations of primary antibodies are used; one using SCP3, H1t and SCP1, another one using SCP3 and STRA8. *Early and late pachytene nuclei cannot be unambiguously differentiated in the absence of H1t staining, and are therefore merged for counting and signal quantification.

Fig. 2

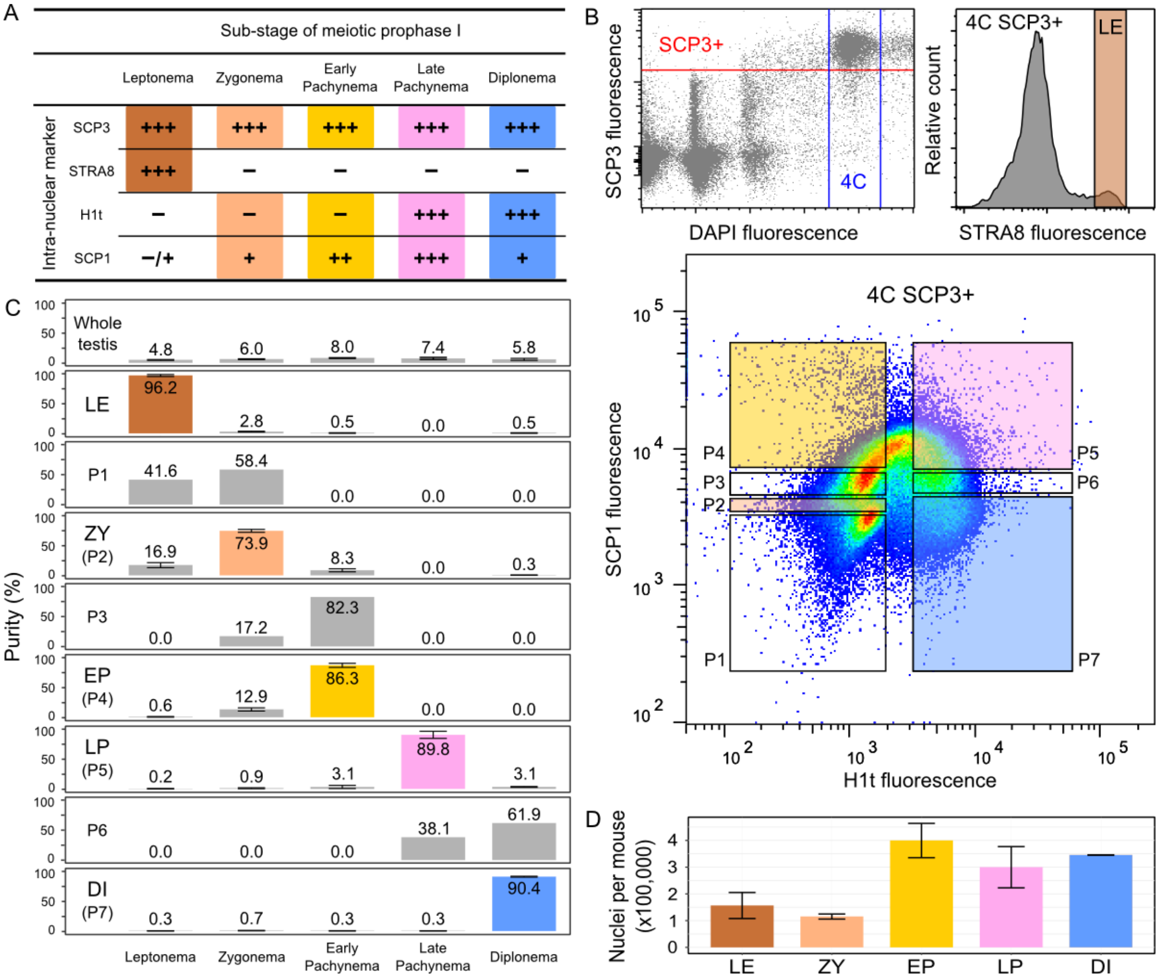

Intra-nuclear marker	Leptonema	Zygonema	Early Pachynema	Late Pachynema	Diplonema
SCP3	+++	+++	+++	+++	+++
STRA8	+++	−	−	−	−
H1t	−	−	−	+++	+++
SCP1	−/+	+	++	+++	+

Fig 2: Experimental design for isolating stage-specific spermatocyte nuclei.

(A) Signal strength of intra-nuclear markers across meiotic sub-stages observed in immunofluorescence staining. Signal strength is classified as absent (–), very weak (–/+), weak (+), medium (++), or strong (+++). Combinatorial markers for isolating stage-specific nuclei are highlighted. (B) Flow cytometric strategies for isolating populations of stage-specific nuclei. Meiotic 4C nuclei are gated by DAPI and SCP3 signals (top left). Stage-specific nuclei are sorted into populations based on combinatorial signals of intra-nuclear markers in two separate sorts; one using antibodies against STRA8 for leptonema (top right), and the other one using antibodies against H1t and SCP1 for seven populations

(P1 to P7) (bottom). (C) Distributions and purities of each specific type of nuclei in whole-testis and in sorted populations. The five selected populations of leptonema, zygonema, early pachynema, late pachynema, and diplonema are highlighted as LE, ZY, EP, LP, and DI, respectively. Purities (mean with standard error) of these populations are derived from two or three independent sorts. (D) Numbers of nuclei in each sub-population collected in an adult mouse. Data (mean with standard error) are derived from two independent sorts.

Fig. 3

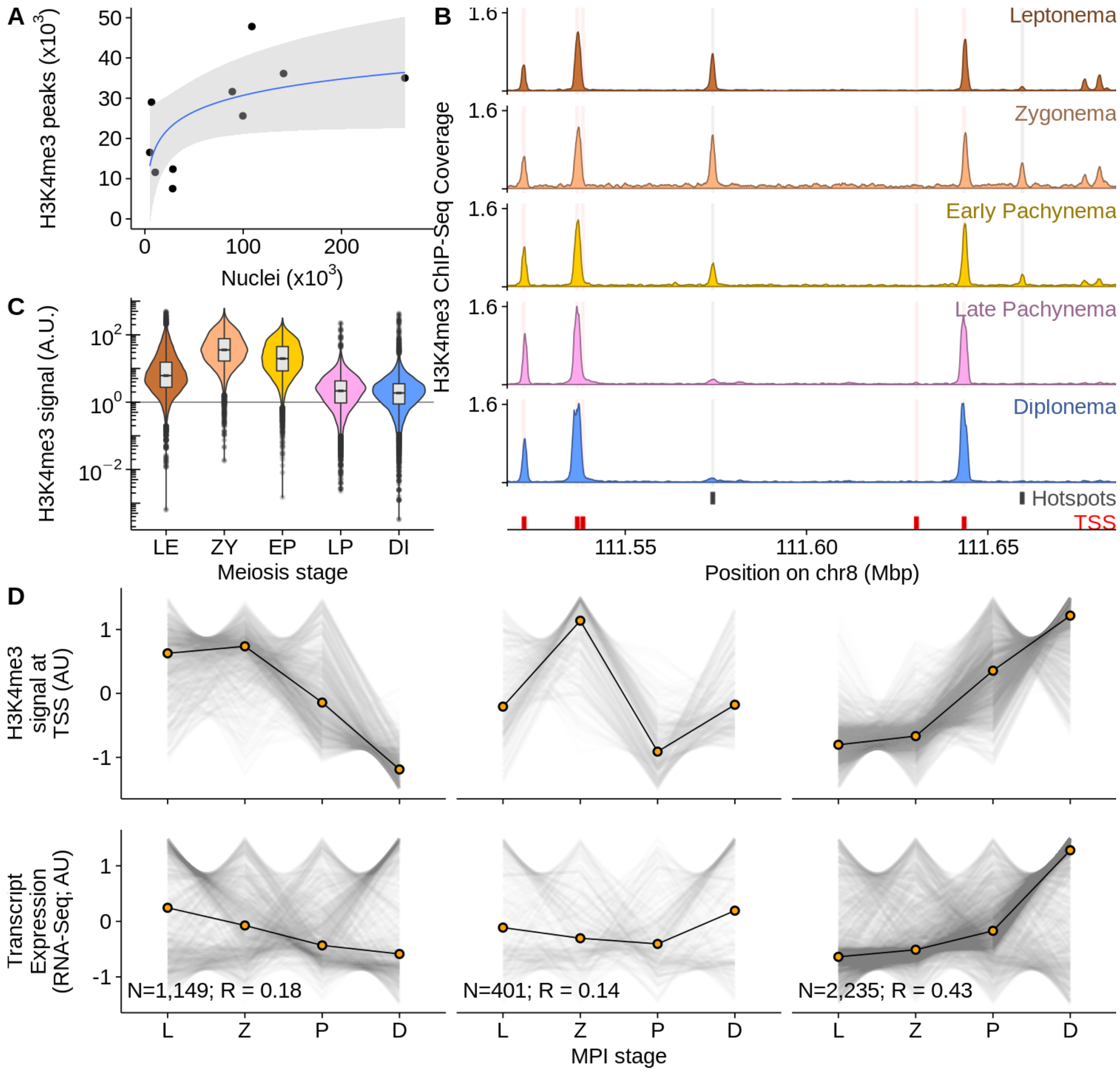

Fig 3: H3K4me3 dynamics across meiotic sub-stages.

(A) Numbers of starting nuclei and H3K4me3 peaks detected in stage-specific H3K4me3-ChIP-Seq. (B) H3K4me3 dynamics at different genomic elements in five sorted sub-populations of meiotic nuclei. (C) H3K4me3 dynamics at DSB hotspots across five meiotic sub-stages. Normalized H3K4me3 signals at DSB hotspots are relative to those at 99 selected TSSs where H3K4me3 signals are constant through meiosis. (D) Stage-specific H3K4me3 at TSSs recapitulate meiotic gene expression patterns. Genes with only one isoform are selected for this analysis. H3K4me3 profiles at TSSs are grouped into three clusters (top), while the respective mRNA levels are shown in the bottom panel. L = Leptonema, Z = Zygonema, P = Early and Late Pachynema, D = Diplonema.

478 **Fig. 4**

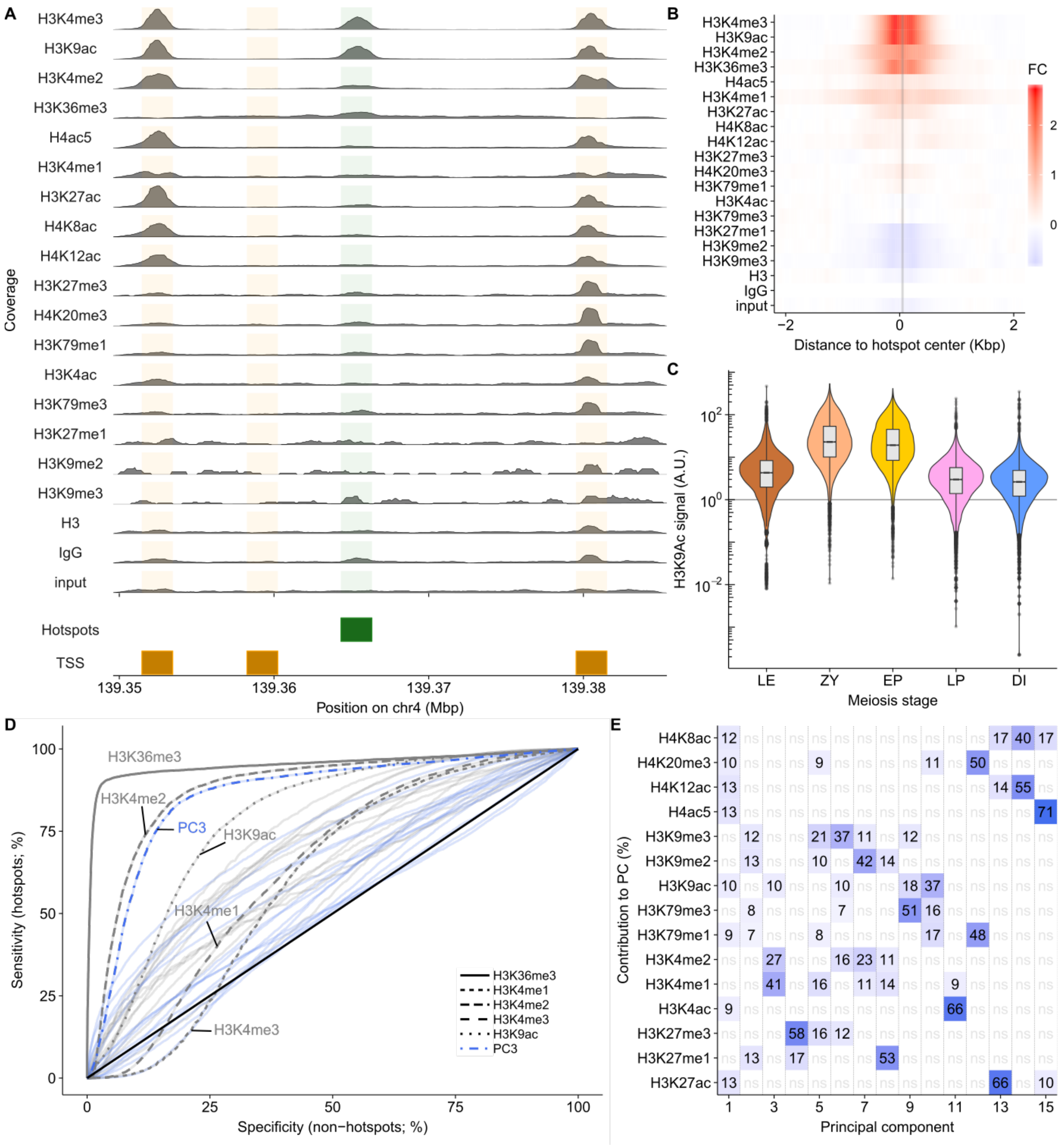

	1		3		5		7		9		11		13		15
H4K8ac	12	ns	ns	ns	ns	ns	ns	ns	ns	ns	ns	ns	17	40	17
H4K20me3	10	ns	ns	ns	9	ns	ns	ns	ns	11	ns	50	ns	ns	ns
H4K12ac	13	ns	ns	ns	ns	ns	ns	ns	ns	ns	ns	ns	14	55	ns
H4ac5	13	ns	ns	ns	ns	ns	ns	ns	ns	ns	ns	ns	ns	ns	71
H3K9me3	ns	12	ns	ns	21	37	11	ns	12	ns	ns	ns	ns	ns	ns
H3K9me2	ns	13	ns	ns	10	ns	42	14	ns	ns	ns	ns	ns	ns	ns
H3K9ac	10	ns	10	ns	ns	10	ns	ns	18	37	ns	ns	ns	ns	ns
H3K79me3	ns	8	ns	ns	ns	7	ns	ns	51	16	ns	ns	ns	ns	ns
H3K79me1	9	7	ns	ns	8	ns	ns	ns	ns	17	ns	48	ns	ns	ns
H3K4me2	ns	ns	27	ns	ns	16	23	11	ns	ns	ns	ns	ns	ns	ns
H3K4me1	ns	ns	41	ns	16	ns	11	14	ns	ns	9	ns	ns	ns	ns
H3K4ac	9	ns	ns	ns	ns	ns	ns	ns	ns	ns	66	ns	ns	ns	ns
H3K27me3	ns	ns	ns	58	16	12	ns	ns	ns	ns	ns	ns	ns	ns	ns
H3K27me1	ns	13	ns	17	ns	ns	ns	53	ns	ns	ns	ns	ns	ns	ns
H3K27ac	13	ns	ns	ns	ns	ns	ns	ns	ns	ns	ns	ns	66	ns	10

479

480

481 **Fig 4: Histone modifications at DSB hotspots.**

482 (**A**) Distributions of histone marks along a genomic region. Locations of DSB
483 hotspots are shaded in green, TSS in orange. (**B**) Histone marks are enriched at
484 DSB hotspots. Red depicts enrichment relative to IgG, blue is depletion. (**C**)
485 H3K9ac dynamics at DSB hotspots across five meiotic sub-stages. **(D-E)**
486 Principal component analysis using histone marks can distinguish DSB hotspots

from PRDM9-independent H3K4me3 sites. **(D)** Histone modifications can distinguish DSB hotspots from other H3K4me3 sites. An ROC curve for each histone mark (grey) or PC (blue) is shown. Selected histone modifications and PC3 are highlighted. **(E)** Contributions of histone marks to each PC. Only marks that contribute more than expected are shown. Deeper blue indicates a stronger contribution (numbers show percent contribution).

Methods

Mouse strains

C57BL/6J (B6) mice were either obtained from The Jackson Laboratory (Stock no. 000664) or bred in-house. All experiments were done on adult mice (≥ 8 weeks of age).

Antibodies

The following antibodies were used for primary immunofluorescence staining: anti-SCP3 (D-1) (Santa Cruz, sc-74569), anti-STRA8 (Abcam, ab49602), anti-H1t (a gift from Mary Ann Handel and a custom-made antibody), and anti-SCP1 [Biotin] (Novus Biologicals, NB300-229B).

The following antibodies were used for secondary immunofluorescence staining: goat anti-mouse IgG conjugated with Cy3 (Jackson ImmunoResearch, 115-167-003), goat anti-rabbit IgG conjugated with FITC (Jackson ImmunoResearch, 115-097-003), goat anti-mouse IgG conjugated with DyLight488 (Abcam, ab98757), goat anti-rabbit IgG conjugated with Cy3 (Jackson ImmunoResearch, 111-165-003), goat anti-guinea pig IgG conjugated with Alexa Fluor 488 (Thermo Fisher Scientific, A-11073), streptavidin conjugated with Alexa Fluor 647 (Thermo Fisher Scientific, S21374).

The following antibodies were used for ChIP: anti-H3K4me3 (Abcam, ab8580), anti-H3K9ac (Active Motif, 39918), anti-H3K4me2 (Active Motif, 39914), anti-H3K36me3 (Active Motif, 61102), anti-H4ac5 (Millipore, 06-946), anti-H3K4me1 (Abcam, ab8895), anti-H3K27ac (Abcam, ab177178), anti-H4K8ac (Abcam, ab15823), anti-H4K12ac (Active Motif, 39928), anti-H3K27me3 (Millipore, 07-449), anti-H4K20me3 (Millipore, 07-463), anti-H3K79me1 (Abcam, ab2886), anti-H3K4ac (Abcam, ab176799), anti-H3K79me3 (Abcam, ab2621), anti-H3K9me2 (Abcam, ab1220), anti-H3K9me3 (Active Motif, 39766), anti-H3K27me1

(Millipore, 07-448), anti-H3 (Abcam, ab1791), normal rabbit IgG (Millipore, 12-370).

Nuclei preparation

Testes from adult mice were de-capsulated and fixed with 1% formaldehyde for 10 min followed by 5 min of quenching at RT. Fixed tissues were homogenized and filtered through a 70- or 100-μm cell strainer. After washing with chilled 1 x PBS, nuclei were extracted using nucleus extraction buffer (15 mM Tris-HCl pH 7.4, 0.34 M sucrose, 15 mM NaCl, 60 mM KCl, 0.2 mM EDTA, 0.2 mM EGTA) on ice for 5 min and were homogenized with 20 strokes with loose pestle followed by 10 strokes with tight pestle. Nuclei were filtered through a 40-μm cell strainer and resuspended in chilled PBTB buffer (1 x PBS with 0.1% Triton X-100, 5% BSA and protease inhibitor).

Immunofluorescence staining

Nuclei were incubated in 10% of normal serum at RT for 10 min. This blocking step helps reduce non-specific binding of antibodies. Nuclei were then labelled with different combinations of primary antibodies (1 μg of antibodies to 11 million events) in 10% of normal serum at 20°C for 40 min. Nuclei were washed, resuspended in PBTB, blocked with serum, and then labelled with secondary antibodies (1:250 dilution) in 10% of normal serum at 20°C for 30 min. Controls for each secondary antibody were also prepared for setting up the threshold of background fluorescent signal for FACS. Nuclei were washed, resuspended in PBTB, and stored at 4°C until sorting.

Quantification of immunofluorescence signal intensity

Nuclei isolated from whole-testis were stained with antibodies against SCP3 and STRA8 or with antibodies against SCP3, H1t and SCP1, and subsequently with secondary antibodies as described. Immunofluorescence-labelled nuclei were spread on microslides, stained with mounting medium with DAPI (Vetashield), sealed with cover slips, and viewed using fluorescence microscopy.

Immunofluorescence signals of each marker were quantified using Volocity 6.2.1 (PerkinElmer). 4C nuclei were identified using signals from the DAPI channel by excluding objects with size < 40 μm^2. Touching objects were separated using the parameter of 30–50 μm^2. Stage-specific nuclei in MPI were characterized by the presence of SCP3 signal and by the patterning of synaptonemal complex[12]. Signals from all channels were recorded and exported for signal quantification.

Isolation of meiotic sub-populations with FACS

Nuclei were filtered through a 40-μm cell strainer, and stained with DAPI for 30 min or longer at RT before sorting. All sorting experiments were performed on either a BD FACSAria II or a BD FACSAria Fusion flow cytometer at a flow rate of ~20,000 events/sec. Singlets were gated using both forward scatter and side scatter. Nuclei from primary spermatocytes (4C) were gated based on DNA content deduced from the DAPI signal, and sorted into populations of interest based on fluorochrome intensity into collection tubes containing PBTB. Sorted nuclei were collected by centrifugation. Nuclei were examined under microscope and counted with a hemocytometer. Finally, excess buffer was removed and nuclei pellets were stored at –80°C.

Assessment of purity of sorted populations

An aliquot of nuclei suspension from each sorted population was spread on microslides, further stained with mounting medium with DAPI (Vectashield), and sealed with coverslips for purity examination. An average of 208 nuclei from each sorted population were checked at 400X magnification using immunofluorescence microscopy. The staging was primarily accessed by the patterning of SCP3[12] and further confirmed by signals of STRA8 or of H1t and SCP1 accordingly.

Chromatin extraction

Chromatin extracted for ChIP-Seq was either sheared by sonication or Micrococcal nuclease (MNase) digestion. Chromatin for all H3K4me3-ChIP-Seq for studying histone dynamics in stage-specific populations was sheared by sonication, whereas ChIP-Seq for identifying histone marks at hotspots were performed on MNase-digested chromatin. Experimental procedures are listed below in detail.

Shearing chromatin by sonication:

Frozen nuclei pellets were thawed at RT for 10 min. Nuclei were lysed with Lysis buffer 1 (0.25% Triton X-100, 10 mM EDTA, 0.5 mM EGTA, 10 mM Tris-HCl pH 8) and incubated at RT for 10 min. Nuclei pellets were subsequently washed with Lysis buffer 2 (200 mM NaCl, 1 mM EDTA, 0.5 mM EGTA, 10 mM Tris-HCl pH 8) and lysed with RIPA buffer (10 mM Tris-HCl pH 8, 1 mM EDTA, 0.5 mM EGTA, 1% Triton X-100, 0.1% sodium deoxycholate, 0.1% SDS, 140 mM NaCl plus protease inhibitor). Chromatin was sheared into ~500–1000 bp fragments by sonication using Bioruptor (diagenode). Chromatin concentration was measured using a Qubit dsDNA HS Assay Kit (Thermo Fisher).

MNase digestion:

Frozen nuclei pellets were thawed at RT for 10 min. Nuclei pellets were resuspended with MNase buffer (50 mM Tris-HCl pH 8, 1 mM $CaCl_2$, 4 mM $MgCl_2$, 4% NP-40 plus protease inhibitor). MNase digestion was performed in a concentration of 3U MNase (USB, Affymetrix) per one million nuclei at 37°C for 5 min. The reaction was stopped by adding a final concentration of 10 mM EDTA and incubated at 4°C for 5 min. Chromatin was pelleted and resuspended in RIPA buffer. Chromatin concentration was measured.

Chromatin Immunoprecipitation

Chromatin was immunoprecipitated with 0.8–5 μg antibodies (or 5 μl unpurified serum) in 0.5–1 ml RIPA buffer at 4°C overnight (see Supplementary Table 1 for details). The immuno-complexes were captured using 20–75 μl Dynabeads Protein G (30 mg/ml, Novex) at 4°C for 2 hr. The beads were washed with buffers previously described[26]. ChIPed DNA was eluted using a IPure kit v2 (diagenode).

Sequencing library construction

ChIP-seq libraries were constructed with a KAPA Hyper Prep Kit (Kapa Biosystems) following steps for generating 1 μg of library DNA. DNA libraries were cleaned up with an Agencourt AMPure XP system (Beckman Coulter). The DNA concentration and fragment size of these libraries were measured with a Qubit dsDNA HS Assay Kit (Thermo Fisher) and an Agilent High Sensitivity DNA Kit (Agilent), respectively.

High throughput DNA sequencing

DNA sequencing was performed on the Illumina HiSeq 2500 or HiSeq X. Sequencing tags were aligned to the mouse mm10/NCBI38 reference genome using BWA mem 0.7.12[47].

Strength estimation

NCIS[48] was used to estimate the contribution of background to each sequencing library. The H3K4me3/H3K9ac strength was calculated for each interval as the number of sequencing reads are less than the NCIS-corrected number of input reads.

Inter-sample normalization using “stable” promoters

The H3K4me3/H3K9ac signal at the central ± 1 Kbp region around GENCODE transcript 5’ ends (TSS) was quantified (as described above) from ChIP-Seq reads in each of the five meiotic populations. TSS that overlapped a DSB hotspot, TSSs with a negative strength after correction and TSS with the strongest (1%) and weakest (15%) H3K4me3 signal at each stage were discarded. The log2 ratio of H3K4me3 was calculated at each TSS between all pairs of stages. TSSs with an absolute log2 (fold-change) ≤ 1.2 between all stages were retained. This resulted in 99 TSSs for H3K4me3 and 93 TSSs for H3K9ac. The strength of each histone mark was then normalized by dividing by the median signal at the respective set of stable TSSs.

Correlating H3K4me3 profiles at TSSs with mRNA expression levels

We used RNA-Seq data from spermatocyte populations obtained by classical cell-sorting to quantify gene expression[33]. Gene expression at GENCODE vM18 transcripts was quantified for each RNA-Seq dataset using kallisto 0.42.1 (kallisto quant --single -l 36 -b 100). Only transcripts with maximal expression > 1 tags per million (TPM), with at least a 2-fold change in expression and with non-zero expression and H3K4me3 signals at all stages were considered for subsequent analysis. To minimize the confounding effects of multiple isoforms, only TSS with a single transcript in this list were retained.

The temporal expression profile for each transcript was described as a four unit vector (Leptonema, Zygonema, Pachynema, Diplonema). Similarly, a temporal profile of H3K4me3 at the TSS was generated. We averaged the Early Pachnema and Late Pachynema H3K4me3 signals to allow direct comparison with the RNA-Seq data.

The overall correlation between H3K4me3 and gene expression was calculated by concatenating all gene expression vectors and comparing with a concatenated vector of H3K4me3. To calculate the expected random correlation, we shuffled the order of each 4-unit transcript H3K4me3 vector before concatenation. 10,000 iterations of this process were performed.

k-means clustering was used to group similar H3K4me3 temporal profiles and to compare each set to gene expression. We used an implementation of the gap-statistic to determine the optimal number of clusters (R; factoextra package). 3 clusters were determined as optimal. Within each set of clusters the method described in the previous paragraph was employed to determine the correlation between H3K4me3 and expression temporal profiles and to derive an empirical p-value for this correlation. Clustering by gene expression instead of by H3K4me3 signal gives similar correlations, though the number of clusters can change (data not shown).

Peak calling

Peaks for H3K4me3 ChIP-Seq were called using MACS2 (version 2.1.0.20140616)[49] with default parameters and with a stage-matched input DNA sample as a control. Peaks overlapping DSB hotspots or gene promoters were ascertained using bedtools (version v2.22.1-4-g3ca83fb)[50] after removing blacklisted regions described in[51]. DSB hotspots were defined and reported in previous studies[27]. Transcription start sites (TSSs) were defined as the ± 0.5 Kbp region around GENCODE v11 transcripts[52]. Overlapping TSSs were merged.

Unbiased clustering of H3K4me3 peaks

H3K4me3 ChIP-Seq peaks from all five populations were merged. H3K4me3 strength was calculated (as described above) for each merged peak in each population. The H3K4me3 profile for each peak was described as a five unit vector (LE, ZY, EP, LP, DI) and scaled by subtracting the mean and dividing by the standard deviation. k-means clustering was used to cluster. Five clusters was determined as optimal using the gap-statistic.

Multiple linear regression

Hotspots overlapping a TSS or overlapping a site used for DSB formation in *Prdm9*$^{-/-}$ mice were discarded. Only hotspots with read coverage > 0 for all histone marks were used for regression analyses because we performed regression on the log10 transformed coverage values. The leaps package in R was used to perform an all-subsets regression using the seven histone marks enriched at DSB hotspots.

Principal Component Analysis

All H3K4me3 peaks from LE, ZY, EP and LP were used for analysis. Each interval was resized to ± 250 bp around the center. Sequencing reads for each histone mark were counted at each feature. Input DNA reads were also counted and subtracted from the count for each mark, following NCIS[48] correction. DSB hotspots and GENCODE TSSs were expanded to ± 1,500 bp to determine H3K4me3 peaks that overlapped hotspots and TSSs, respectively. Peaks that overlapped both a hotspot and TSS were discarded as the potential compound signal would confound these analyses. Only autosomal peaks were used. H3K36me3 and H3K4me3 were excluded. The R prcomp command was used for Principal Component Analysis. Variables were scaled to have unit variance and zero centered.

TSSs were split to into Active (TSS(On)) and Inactive (TSS(Off)); active TSS were those upstream of genes expressed in early MPI (expression > 0 TPM at pre-leptotene, leptotene, zygotene or pachytene; gene expression data from RNA-Seq[33]). DSB hotspots were split into two sets by strength; the top 25%; Hot HS and the rest; HS.

ROC curves were built by ranking intervals by the dependent variable. Intervals were ranked either from high to low or from low to high and the ROC with the higher area under the curve was used.

References

1. Handel, M. A., Eppig, J. J. & Schimenti, J. C. Applying 'Gold Standards' to In-Vitro-Derived Germ Cells. *Cell* **157,** 1257–1261 (2014).
2. Bellve, A. R., Cavicchia, J. C. & Millette, C. F. Spermatogenic cells of the prepuberal mouse: isolation and morphological characterization. *J. Cell Biol.* (1977).
3. Goetz, P., Chandley, A. C. & Speed, R. M. Morphological and temporal sequence of meiotic prophase development at puberty in the male mouse. *J. Cell Sci.* **65,** 249–263 (1984).
4. Kluin, P. M., Kramer, M. F. & de Rooij, D. G. Spermatogenesis in the immature mouse proceeds faster than in the adult. *Int. J. Androl.* **5,** 282–294 (1982).
5. Zelazowski, M. J. *et al.* Age-Dependent Alterations in Meiotic Recombination Cause Chromosome Segregation Errors in Spermatocytes. *Cell* **171,** 601–614.e13 (2017).
6. Hogarth, C. A. *et al.* Turning a spermatogenic wave into a tsunami: synchronizing murine spermatogenesis using WIN 18,446. *Biol. Reprod.* **88,** 40–41 (2013).
7. Bastos, H. *et al.* Flow cytometric characterization of viable meiotic and postmeiotic cells by Hoechst 33342 in mouse spermatogenesis. *Cytometry A* **65,** 40–49 (2005).
8. Barchi, M., Geremia, R., Magliozzi, R. & Bianchi, E. Isolation and analyses of enriched populations of male mouse germ cells by sedimentation velocity: the centrifugal elutriation. *Methods Mol. Biol.* **558,** 299–321 (2009).
9. Gaysinskaya, V., Soh, I. Y., Heijden, G. W. & Bortvin, A. Optimized flow cytometry isolation of murine spermatocytes. *Cytometry A* **85,** 556–565 (2014).
10. Bonn, S. *et al.* Cell type–specific chromatin immunoprecipitation from multicellular complex samples using BiTS-ChIP. *Nat. Protoc.* **7,** 978 (2012).
11. Meuwissen, R. L. *et al.* A coiled-coil related protein specific for synapsed regions of meiotic prophase chromosomes. *EMBO J.* **11,** 5091–5100 (1992).

12. Dobson, M. J., Pearlman, R. E., Karaiskakis, A., Spyropoulos, B. & Moens, P. B. Synaptonemal complex proteins: occurrence, epitope mapping and chromosome disjunction. *J. Cell Sci.* **107 (Pt 10),** 2749–2760 (1994).
13. Inselman, A., Eaker, S. & Handel, M. A. Temporal expression of cell cycle-related proteins during spermatogenesis: establishing a timeline for onset of the meiotic divisions. *Cytogenet. Genome Res.* **103,** 277–284 (2003).
14. Mark, M. *et al.* STRA8-deficient spermatocytes initiate, but fail to complete, meiosis and undergo premature chromosome condensation. *J. Cell Sci.* **121,** 3233–3242 (2008).
15. Powers, N. R. *et al.* The Meiotic Recombination Activator PRDM9 Trimethylates Both H3K36 and H3K4 at Recombination Hotspots In Vivo. *PLoS Genet.* **12,** e1006146 (2016).
16. Grey, C. *et al.* In vivo binding of PRDM9 reveals interactions with noncanonical genomic sites. *Genome Res.* **27,** 580–590 (2017).
17. Margolin, G., Khil, P. P., Kim, J., Bellani, M. A. & Camerini-Otero, R. D. Integrated transcriptome analysis of mouse spermatogenesis. *BMC Genomics* **15,** 39 (2014).
18. Sun, F. *et al.* Nuclear localization of PRDM9 and its role in meiotic chromatin modifications and homologous synapsis. *Chromosoma* **124,** 397–415 (2015).
19. Moens, P. B. *et al.* The time course and chromosomal localization of recombination-related proteins at meiosis in the mouse are compatible with models that can resolve the early DNA-DNA interactions without reciprocal recombination. *J. Cell Sci.* **115,** 1611–1622 (2002).
20. Cole, F. *et al.* Homeostatic control of recombination is implemented progressively in mouse meiosis. *Nat. Cell Biol.* **14,** 424–430 (2012).
21. Buard, J., Barthès, P., Grey, C. & de Massy, B. Distinct histone modifications define

initiation and repair of meiotic recombination in the mouse. *EMBO J.* **28,** 2616–2624 (2009).

22. Moens, P. B. Histones H1 and H4 of surface-spread meiotic chromosomes. *Chromosoma* **104,** 169–174 (1995).
23. Adli, M. & Bernstein, B. E. Whole-genome chromatin profiling from limited numbers of cells using nano-ChIP-seq. *Nat. Protoc.* **6,** 1656–1668 (2011).
24. Bernstein, B. E. *et al.* Genomic maps and comparative analysis of histone modifications in human and mouse. *Cell* **120,** 169–181 (2005).
25. ENCODE Project Consortium. An integrated encyclopedia of DNA elements in the human genome. *Nature* **489,** 57–74 (2012).
26. Smagulova, F. *et al.* Genome-wide analysis reveals novel molecular features of mouse recombination hotspots. *Nature* **472,** 375–378 (2011).
27. Brick, K., Smagulova, F., Khil, P., Camerini-Otero, R. D. & Petukhova, G. V. Genetic recombination is directed away from functional genomic elements in mice. *Nature* **485,** 642–645 (2012).
28. John, S. *et al.* Chromatin accessibility pre-determines glucocorticoid receptor binding patterns. *Nat. Genet.* **43,** 264–268 (2011).
29. Landt, S. G. *et al.* ChIP-seq guidelines and practices of the ENCODE and modENCODE consortia. *Genome Res.* **22,** 1813–1831 (2012).
30. Mimitou, E. P., Yamada, S. & Keeney, S. A global view of meiotic double-strand break end resection. *Science* **355,** 40–45 (2017).
31. Wojtasz, L. *et al.* Mouse HORMAD1 and HORMAD2, two conserved meiotic chromosomal proteins, are depleted from synapsed chromosome axes with the help of TRIP13 AAA-ATPase. *PLoS Genet.* **5,** e1000702 (2009).
32. Keeney, S., Lange, J. & Mohibullah, N. Self-Organization of Meiotic Recombination

Initiation: General Principles and Molecular Pathways. *Annu. Rev. Genet.* **48,** 187–214 (2014).

33. Gaysinskaya, V. *et al.* Transient reduction of DNA methylation at the onset of meiosis in male mice. *Epigenetics Chromatin* **11,** 15 (2018).
34. Tibshirani, R., Walther, G. & Hastie, T. Estimating the number of clusters in a data set via the gap statistic. *J. R. Stat. Soc. Series B Stat. Methodol.* **63,** 411–423 (2001).
35. Vastenhouw, N. L. *et al.* Chromatin signature of embryonic pluripotency is established during genome activation. *Nature* **464,** 922–926 (2010).
36. Diagouraga, B. *et al.* PRDM9 Methyltransferase Activity Is Essential for Meiotic DNA Double-Strand Break Formation at Its Binding Sites. *Mol. Cell* **69,** 853–865.e6 (2018).
37. Walker, M. *et al.* Affinity-seq detects genome-wide PRDM9 binding sites and reveals the impact of prior chromatin modifications on mammalian recombination hotspot usage. *Epigenetics Chromatin* **8,** 31 (2015).
38. Getun, I. V. *et al.* Functional Roles of Acetylated Histone Marks at Mouse Meiotic Recombination Hot Spots. *Mol. Cell. Biol.* **37,** (2017).
39. Merker, J. D. *et al.* The histone methylase Set2p and the histone deacetylase Rpd3p repress meiotic recombination at the HIS4 meiotic recombination hotspot in Saccharomyces cerevisiae. *DNA Repair* **7,** 1298–1308 (2008).
40. Yamada, S., Ohta, K. & Yamada, T. Acetylated Histone H3K9 is associated with meiotic recombination hotspots, and plays a role in recombination redundantly with other factors including the H3K4 methylase Set1 in fission yeast. *Nucleic Acids Res.* **41,** 3504–3517 (2013).
41. Lange, J. *et al.* The Landscape of Mouse Meiotic Double-Strand Break Formation,

Processing, and Repair. *Cell* **167,** 695–708.e16 (2016).

42. Yamada, S. *et al.* Genomic and chromatin features shaping meiotic double-strand break formation and repair in mice. *Cell Cycle* **16,** 1870–1884 (2017).
43. Thacker, D., Mohibullah, N., Zhu, X. & Keeney, S. Homologue engagement controls meiotic DNA break number and distribution. *Nature* **510,** 241–246 (2014).
44. Kauppi, L. *et al.* Numerical constraints and feedback control of double-strand breaks in mouse meiosis. *Genes Dev.* **27,** 873–886 (2013).
45. Baker, C. L., Walker, M., Kajita, S., Petkov, P. M. & Paigen, K. PRDM9 binding organizes hotspot nucleosomes and limits Holliday junction migration. *Genome Res.* **24,** 724–732 (2014).
46. Gates, L. A., Foulds, C. E. & O'Malley, B. W. Histone Marks in the 'Driver's Seat': Functional Roles in Steering the Transcription Cycle. *Trends Biochem. Sci.* **42,** 977–989 (2017).
47. Li, H. Aligning sequence reads, clone sequences and assembly contigs with BWA-MEM. *arXiv [q-bio.GN]* (2013).
48. Liang, K. & Keleş, S. Normalization of ChIP-seq data with control. *BMC Bioinformatics* **13,** 199 (2012).
49. Zhang, Y. *et al.* Model-based analysis of ChIP-Seq (MACS). *Genome Biol.* **9,** R137 (2008).
50. Quinlan, A. R. & Hall, I. M. BEDTools: a flexible suite of utilities for comparing genomic features. *Bioinformatics* **26,** 841–842 (2010).
51. Smagulova, F., Brick, K., Pu, Y., Camerini-Otero, R. D. & Petukhova, G. V. The evolutionary turnover of recombination hot spots contributes to speciation in mice. *Genes Dev.* **30,** 266–280 (2016).
52. Mudge, J. M. & Harrow, J. Creating reference gene annotation for the mouse

C57BL6/J genome assembly. *Mamm. Genome* **26,** 366–378 (2015).

53. Ramírez, F., Dündar, F., Diehl, S., Grüning, B. A. & Manke, T. deepTools: a flexible platform for exploring deep-sequencing data. *Nucleic Acids Res.* **42,** W187–91 (2014).

Supplementary Figures

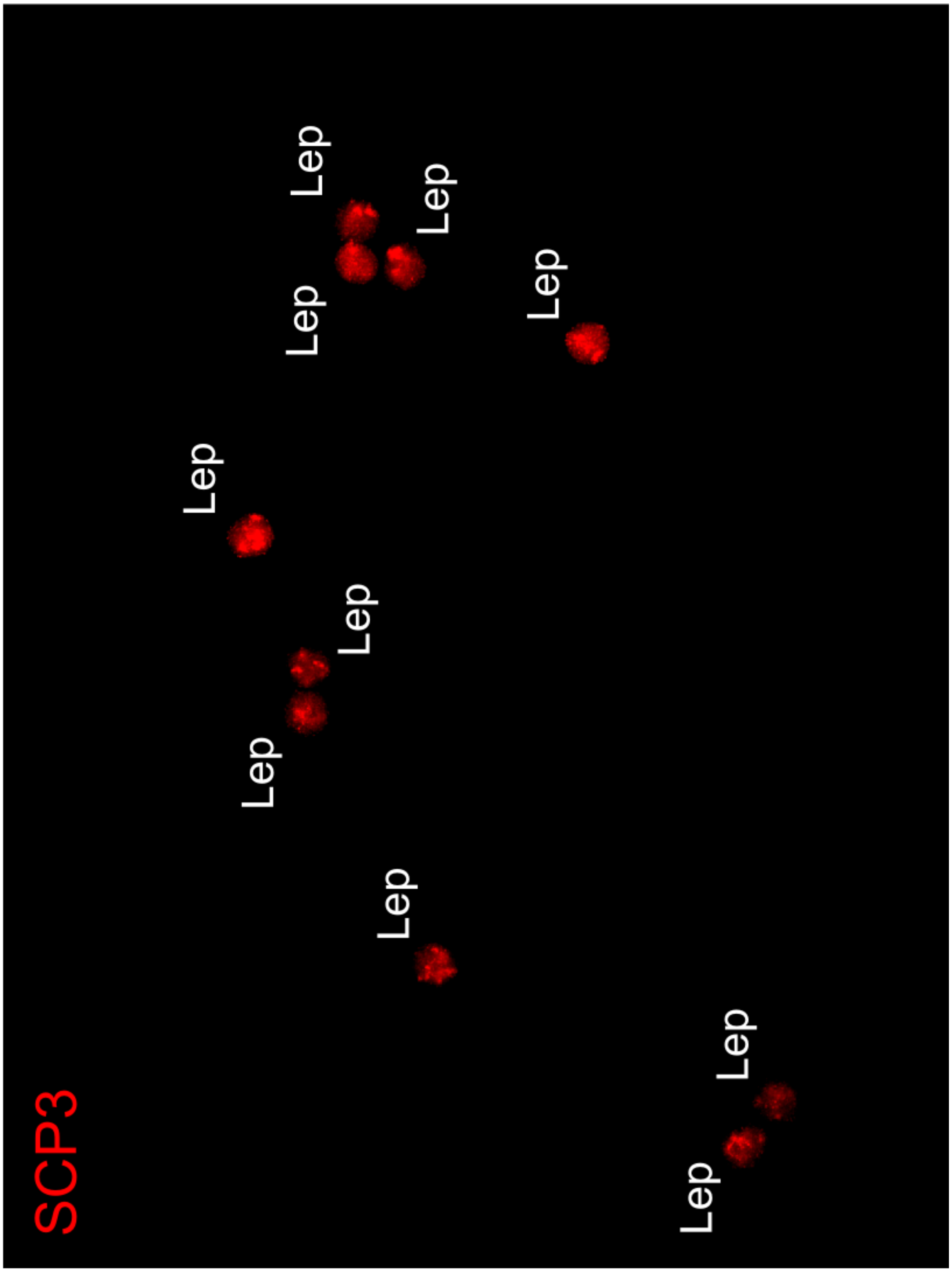

A (i)

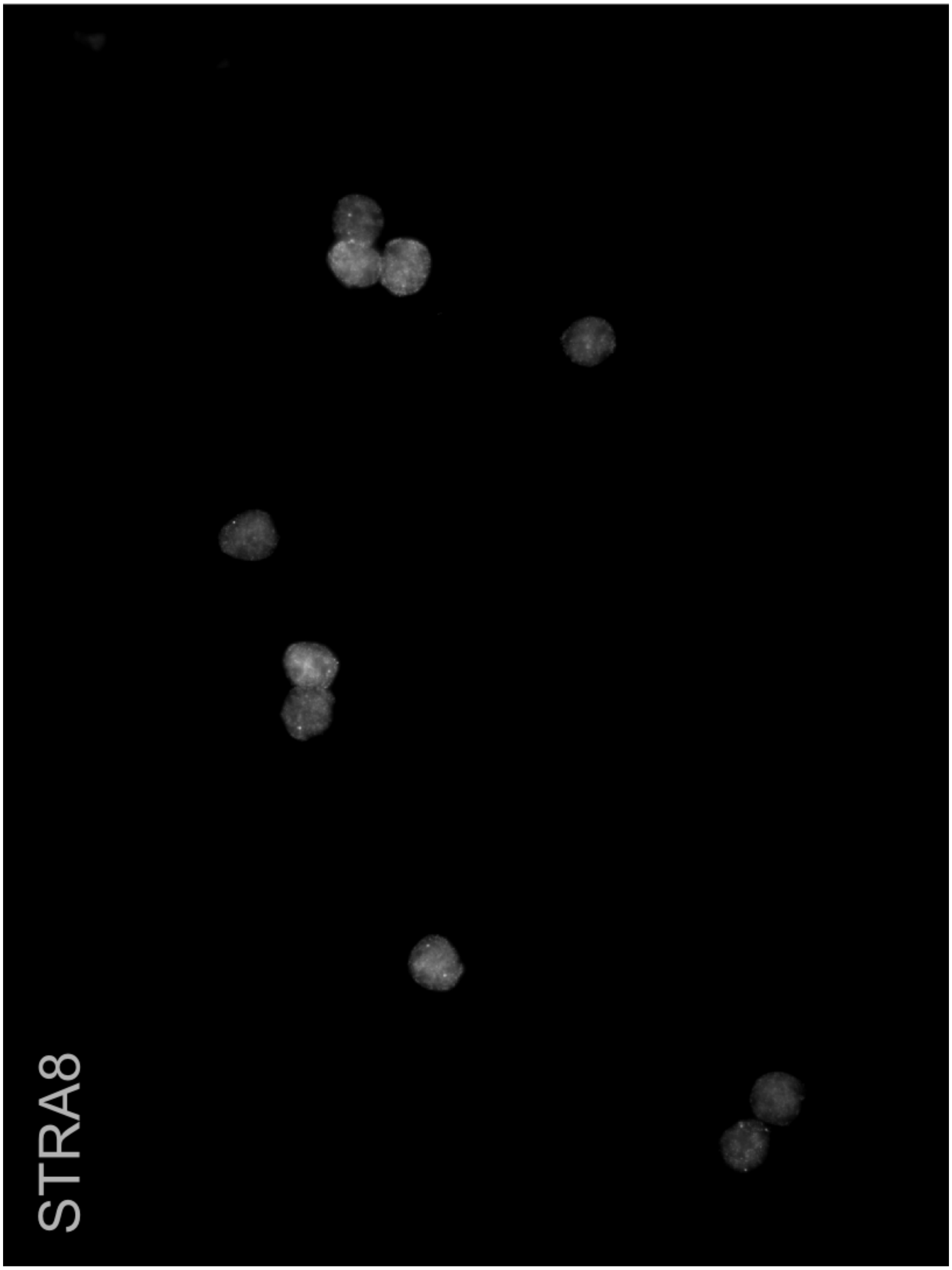

A (ii)

A (iii)

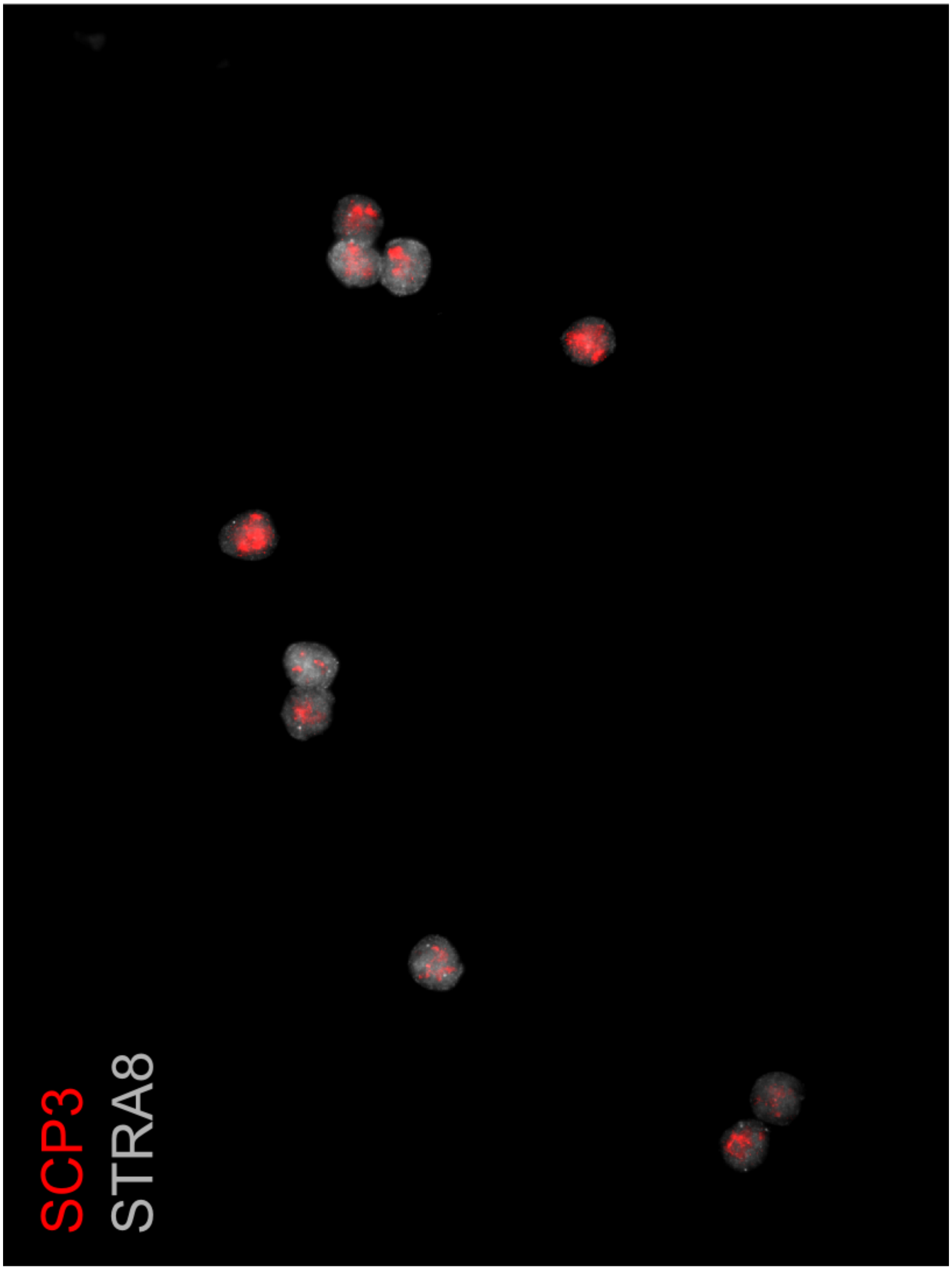

B (i)

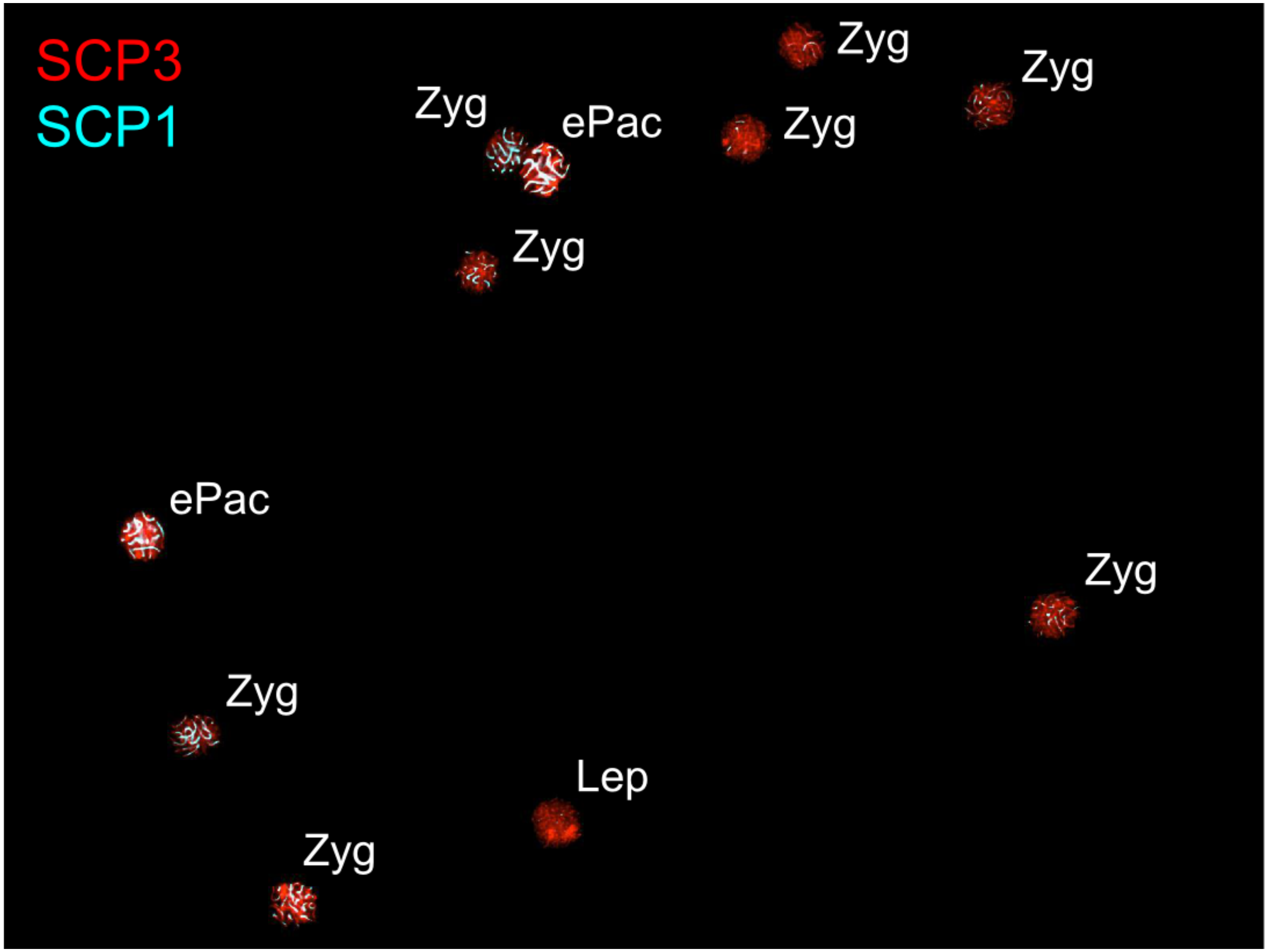

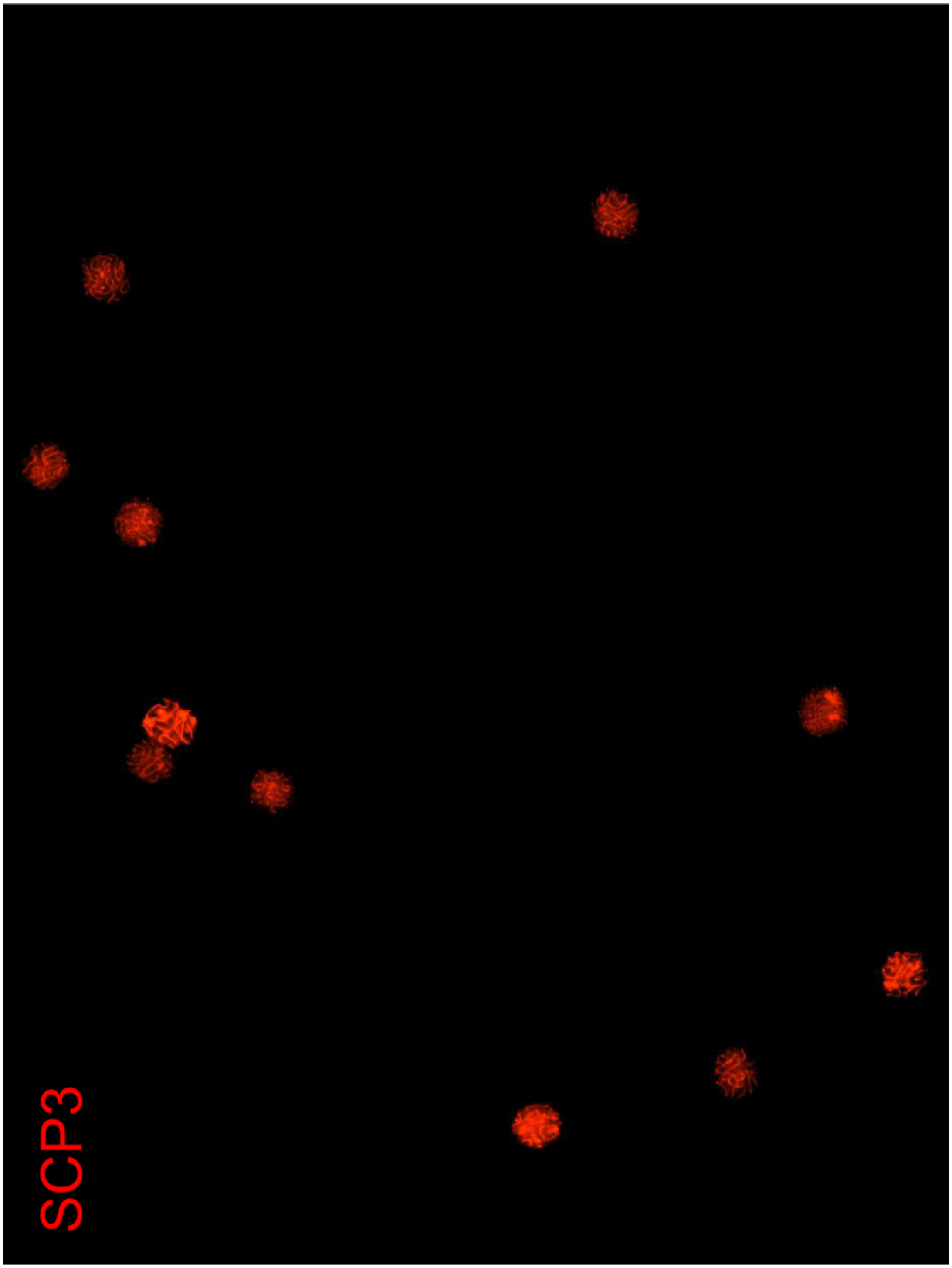

B (ii)

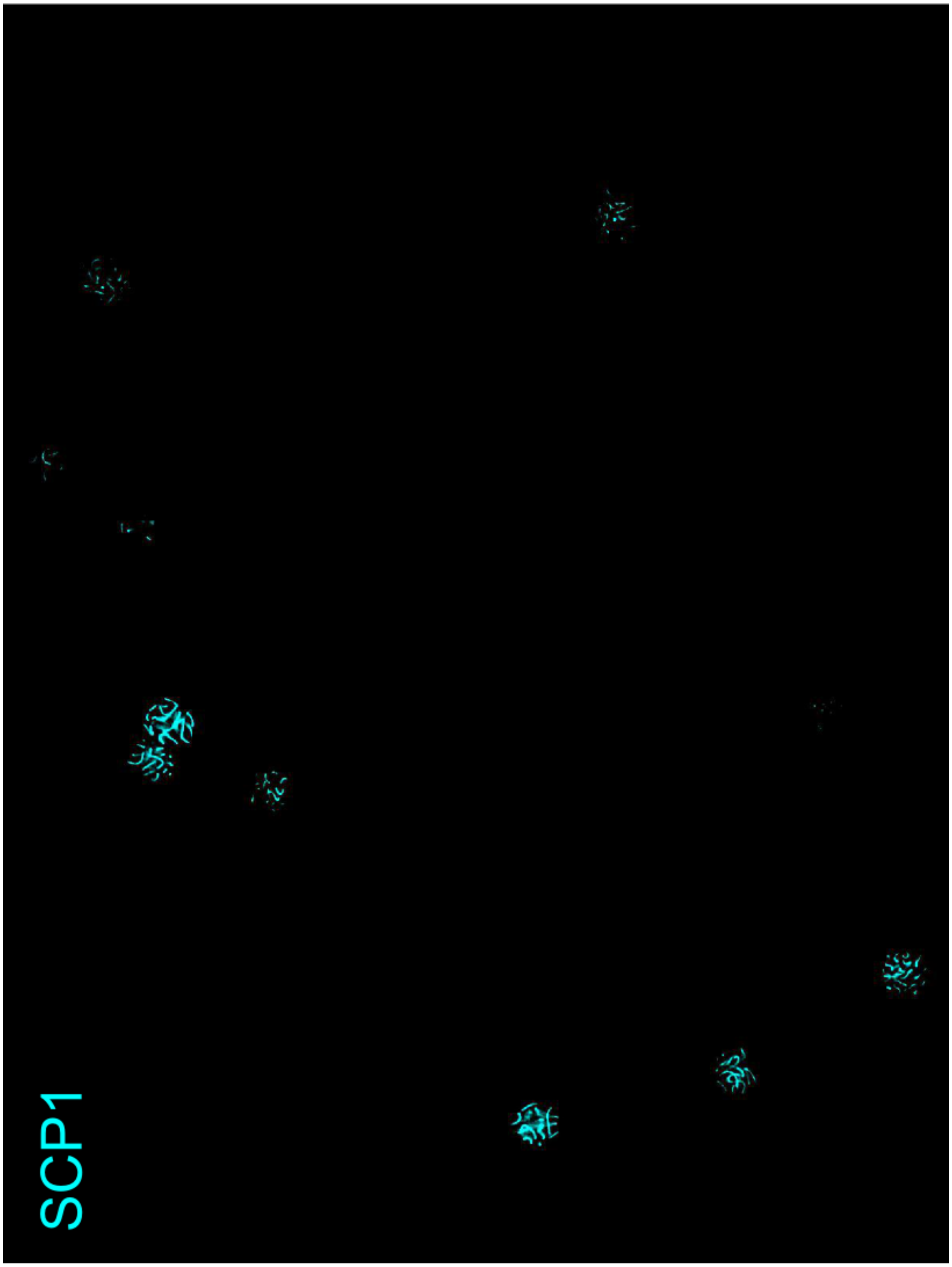

B (iii)

Supplementary Fig 1: Microscopic examination of sorted nuclei after FACS.

Whole-field immunofluorescence images of sorted nuclei in the populations of (A) leptonema and (B) zygonema. Lep=leptonema; Zyg=zygonema; ePac=early pachynema.

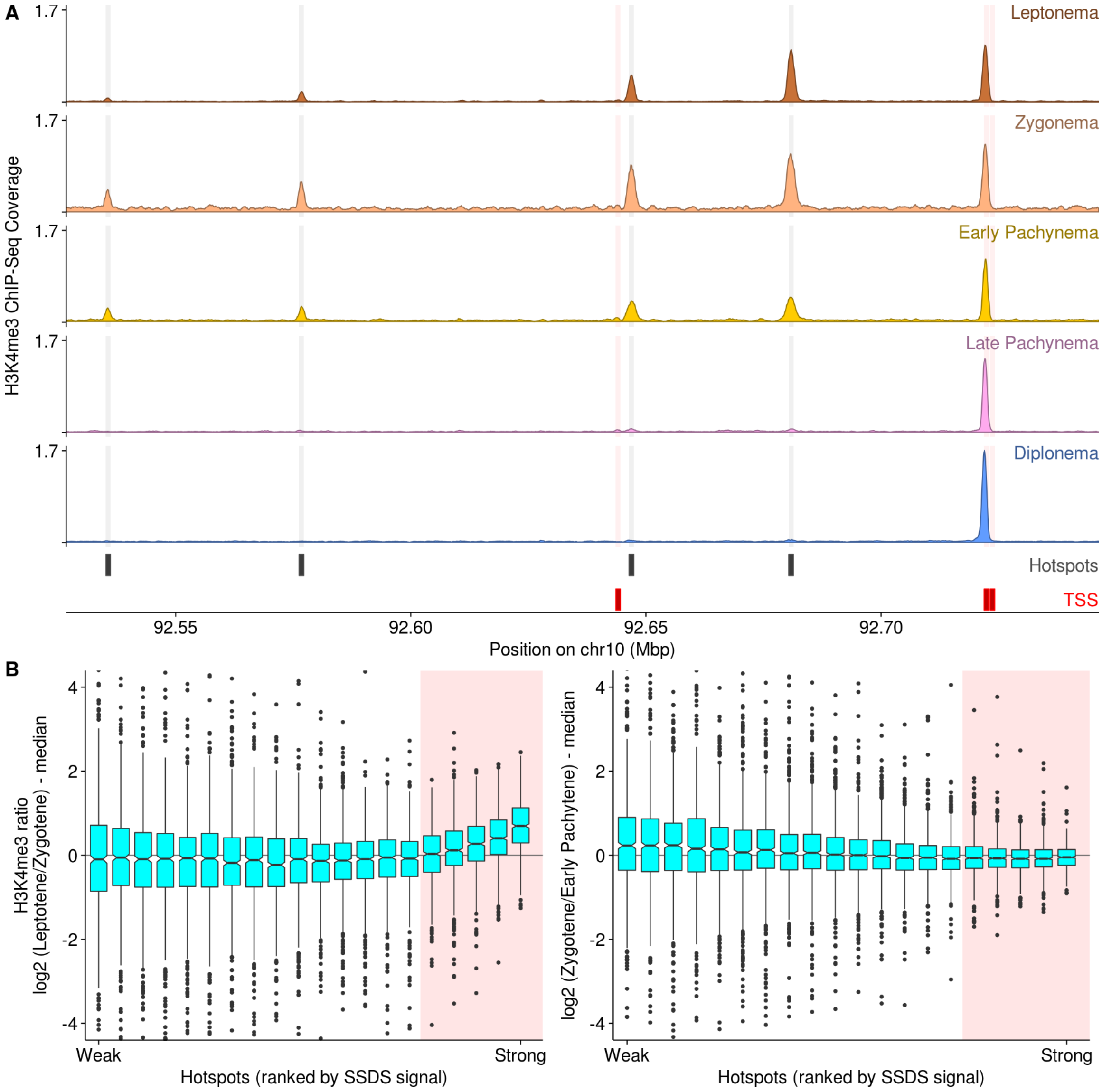

Supplementary Fig 2: H3K4me3 is relatively elevated at stronger DSB hotspots in Leptonema. (A) Snapshot of H3K4me3 at four DSB hotspots. The DSB hotspots are progressively stronger from left to right. At the weakest hotspot (left) the H3K4me3 signal is maximal at Zygonema. At the strongest hotspot (right) the H3K4me3 signal is strongest at Leptonema. (B) Systematic trend towards stronger Leptonema H3K4me3 at stronger DSB hotspots. On the left panel, the H3K4me3 ratio between Leptonema and Zygonema is shown. Red shaded area shows the trend region. This trend is not seen when comparing Zygonema to Early Pachynema H3K4me3.

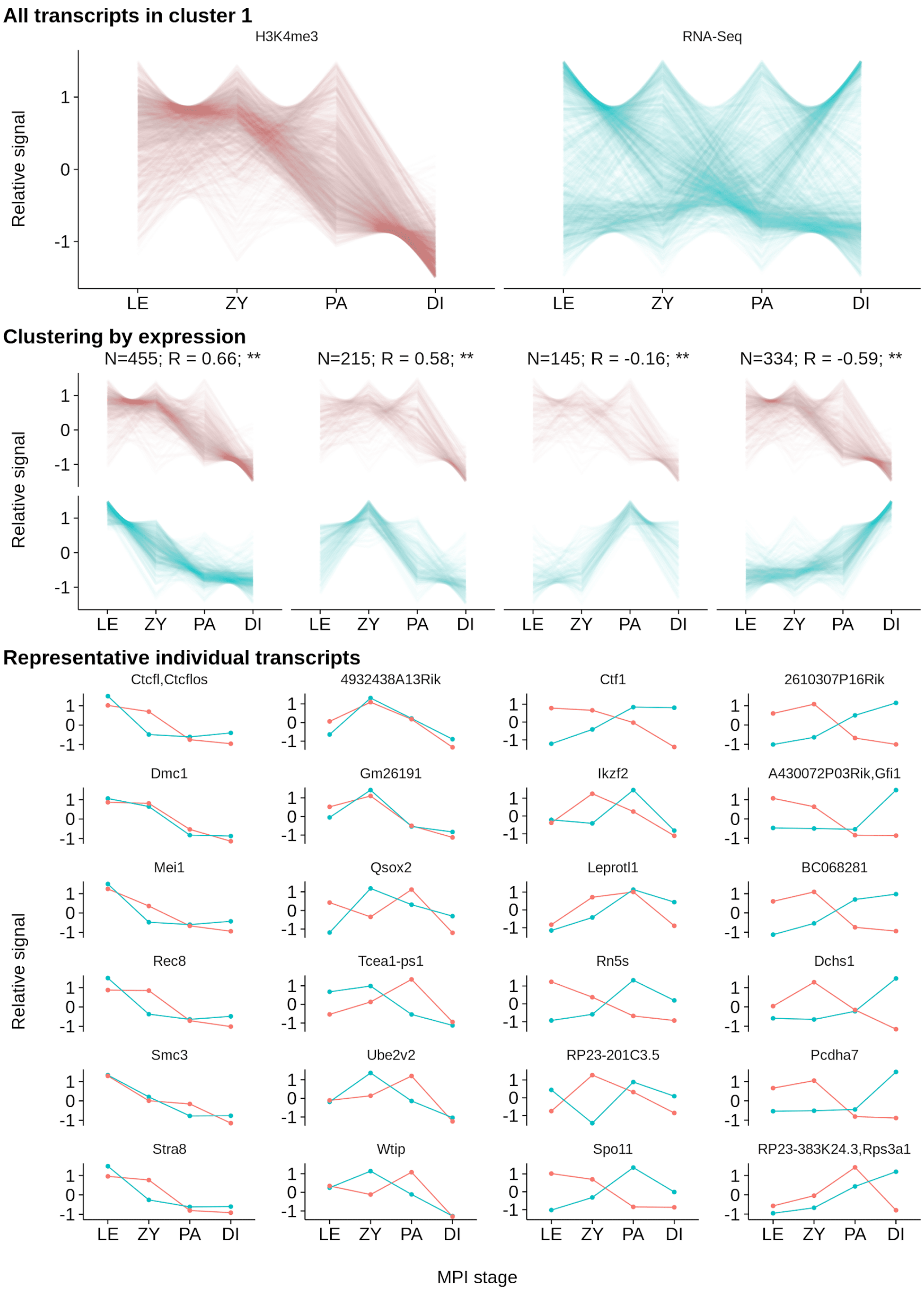
All transcripts in cluster 1
H3K4me3
RNA-Seq
Relative signal
1
0
-1
LE
ZY
PA
DI
Clustering by expression
N=455; R = 0.66; **
N=215; R = 0.58; **
N=145; R = -0.16; **
N=334; R = -0.59; **
Representative individual transcripts
Ctcfl,Ctcflos
4932438A13Rik
Ctf1
2610307P16Rik
Dmc1
Gm26191
Ikzf2
A430072P03Rik,Gfi1
Mei1
Qsox2
Leprotl1
BC068281
Rec8
Tcea1-ps1
Rn5s
Dchs1
Smc3
Ube2v2
RP23-201C3.5
Pcdha7
Stra8
Wtip
Spo11
RP23-383K24.3,Rps3a1
MPI stage

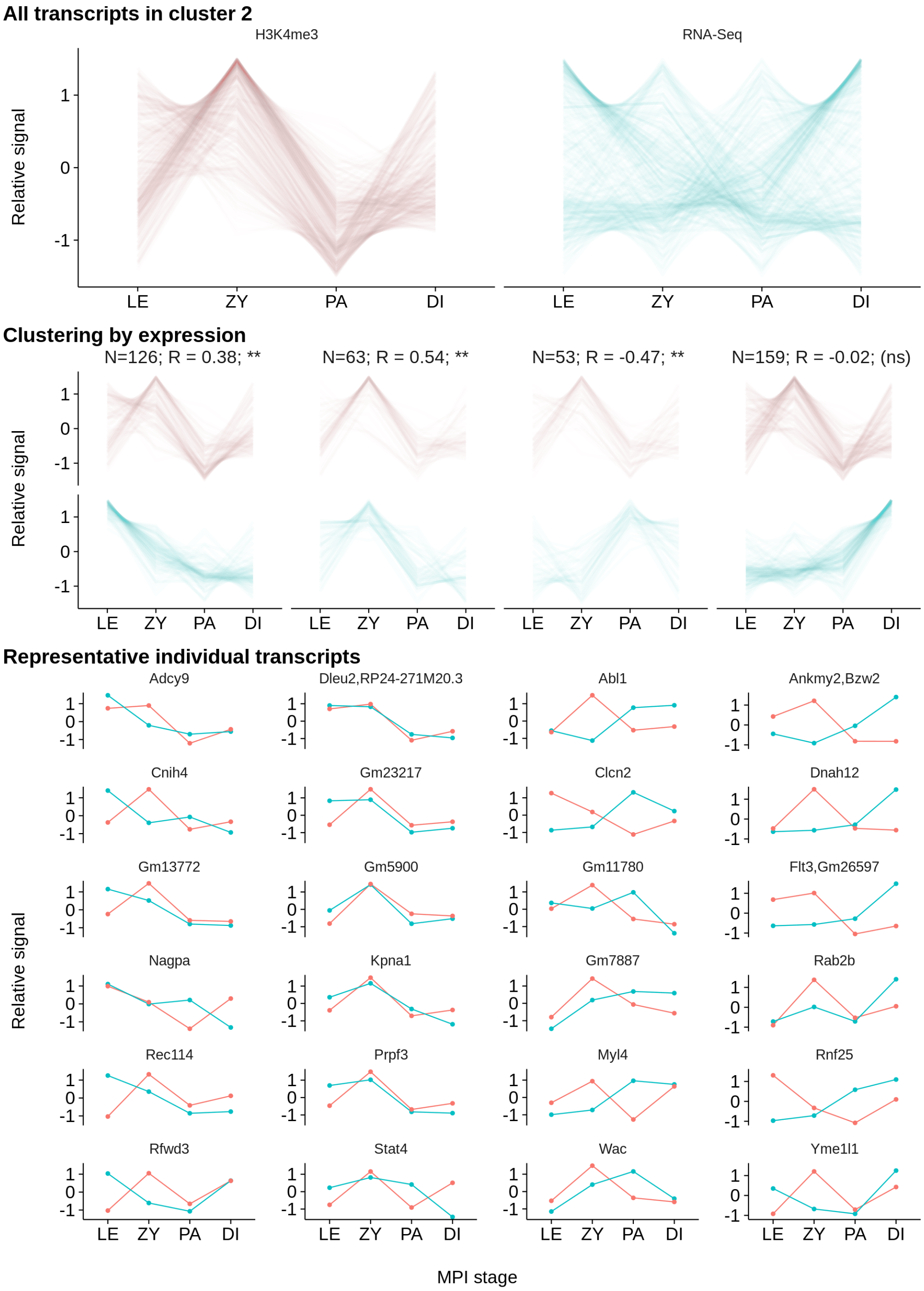
All transcripts in cluster 2
H3K4me3
RNA-Seq
Relative signal
1
0
-1
LE
ZY
PA
DI
Clustering by expression
N=126; R = 0.38; **
N=63; R = 0.54; **
N=53; R = -0.47; **
N=159; R = -0.02; (ns)
Representative individual transcripts
Adcy9
Dleu2,RP24-271M20.3
Abl1
Ankmy2,Bzw2
Cnih4
Gm23217
Clcn2
Dnah12
Gm13772
Gm5900
Gm11780
Flt3,Gm26597
Nagpa
Kpna1
Gm7887
Rab2b
Rec114
Prpf3
Myl4
Rnf25
Rfwd3
Stat4
Wac
Yme1l1
MPI stage

894

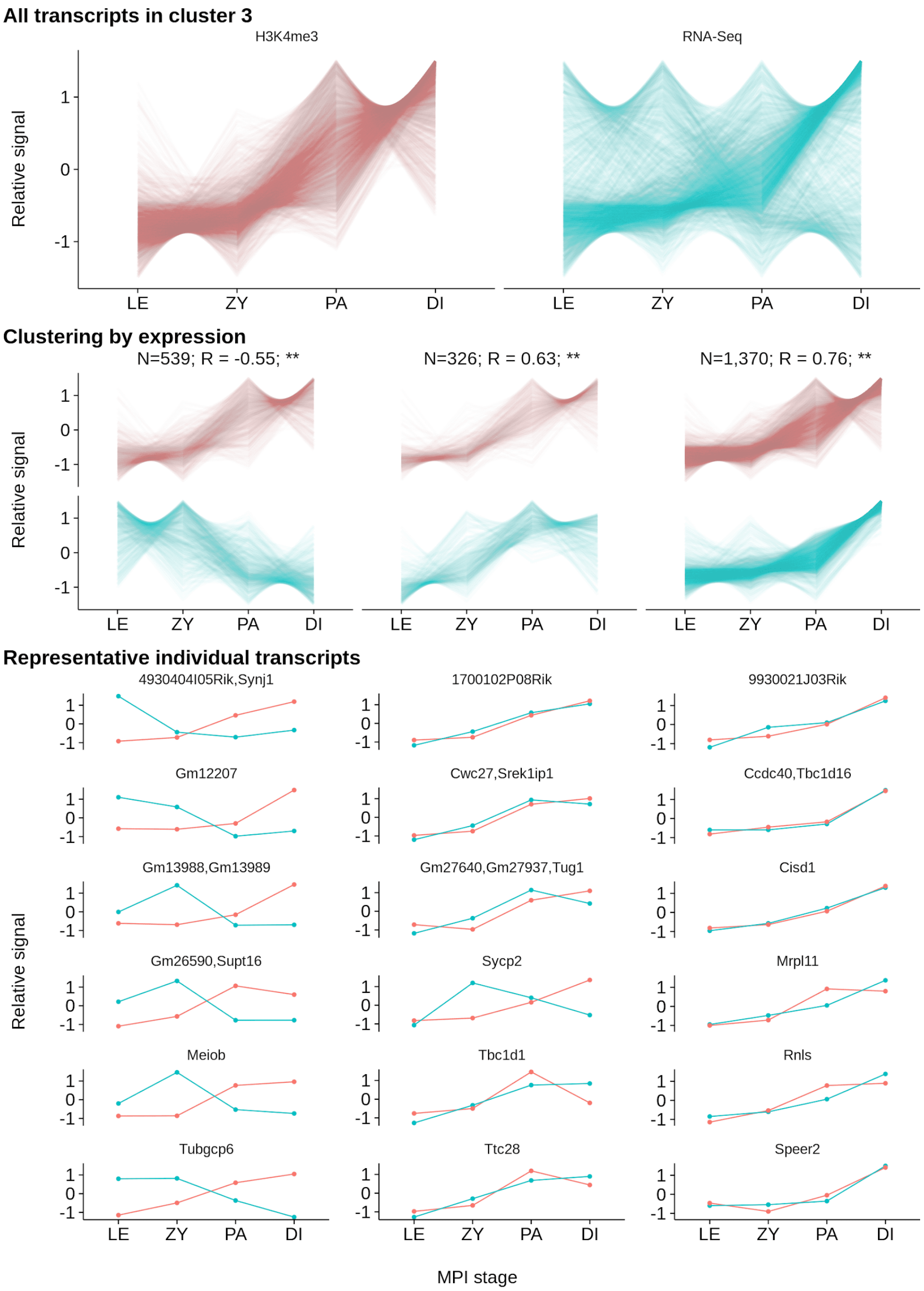

Supplementary Fig 3: H3K4me3 dynamics correlate with gene expression profiles from male juvenile mice.

Each of the four plots represents a single cluster of transcripts from Fig. 2. Throughout, red depicts H3K4me3 ChIP-Seq signal and blue depicts gene expression from RNA-Seq. Each top panels shows all transcripts in the cluster; lines represent individual transcripts. Transcripts were next sub-clustered by gene expression profile (middle panels; k-means clustering; optimal k chosen using gap statistic). Clusters in which profiles correlate more or less than expected are highlighted (* = $P < 0.01$, ** = $P < 0.001$; 1,000 bootstraps of shuffling stages for each gene). Six representative transcripts from each cluster are shown in the lower panel below each cluster. Transcripts of genes known to play a role in MPI were preferentially selected; if < 6 such genes were present in a cluster, the remainder were randomly selected.

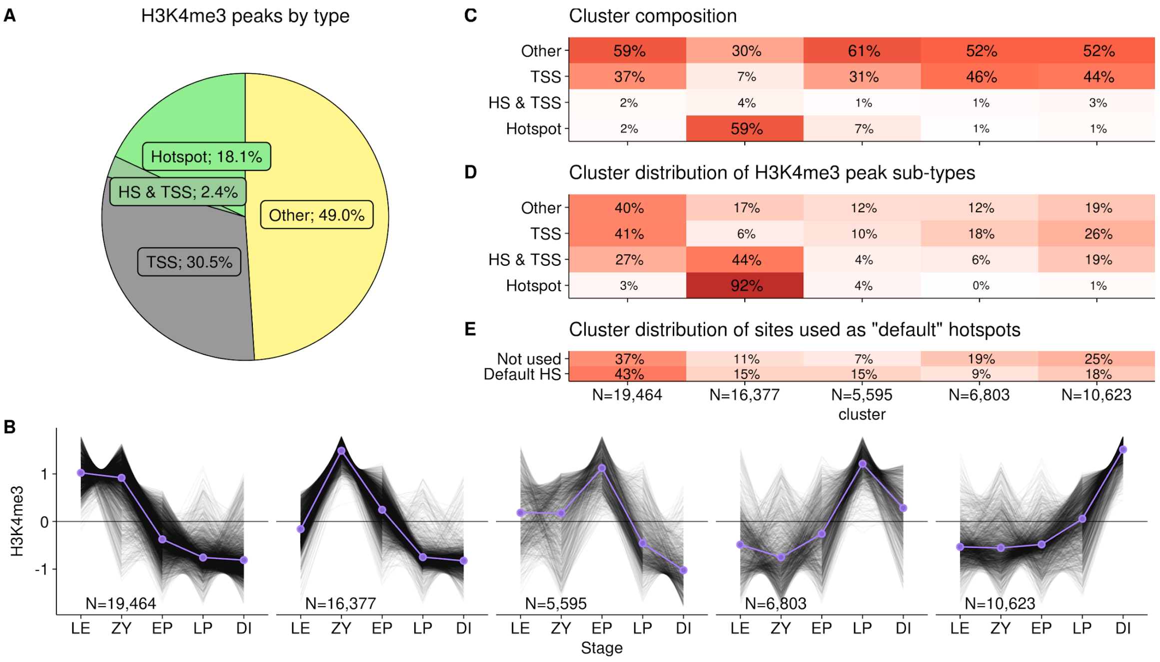

Supplementary Fig 4: Extensive dynamics revealed by unbiased clustering of H3K4me3 peaks. (A) Almost half (49%) of all H3K4me3 peaks occur at sites not defined at DSB hotspots or transcription start sites (TSS). These are classified as "Other". 2.4% of H3K4me3 peaks coincide with both a DSB hotspot and a GENCODE TSS (HS & TSS). (B) Unbiased k-means clustering of MPI H3K4me3 profiles. Each black line represents the MPI profile of an individual H3K4me3 peak. 10,000 randomly chosen profiles are shown. Purple lines depict the mean profile for each cluster. Profiles are normalized by the mean and standard deviation. The optimum number of clusters was identified using the gap statistic (optimum k = 5; range tested = 2 < k < 24). (C) Cluster composition shown as the percentage of each type of H3K4me3 peak within each cluster. Cluster 2 is the only cluster composed primarily of peaks at DSB hotspots. (D) The percentage of peaks of each type across clusters is shown. Notably, 92% of DSB hotspots occur in cluster 2. 44% of HS & TSS peaks also occur in this cluster, suggesting that H3K4me3 at many of these sites is PRDM9-mediated. (E) In mice lacking PRDM9, PRDM9-independent H3K4me3 peaks are used for targeting the DSB machinery. These sites are termed "default hotspots" and are defined as H3K4me3 peaks that coincide with a DSB hotspot in *Prdm9*$^{-/-}$ mice[27]. Default hotspots form more frequently than expected at H3K4me3 peaks that are present in early MPI (cluster 1-3). Peaks with a late dynamic (cluster 4, 5) are used less than expected. The "Not used" peaks are all H3K4me3 peaks that do not coincide with either a PRDM9-defined or a default hotspot.

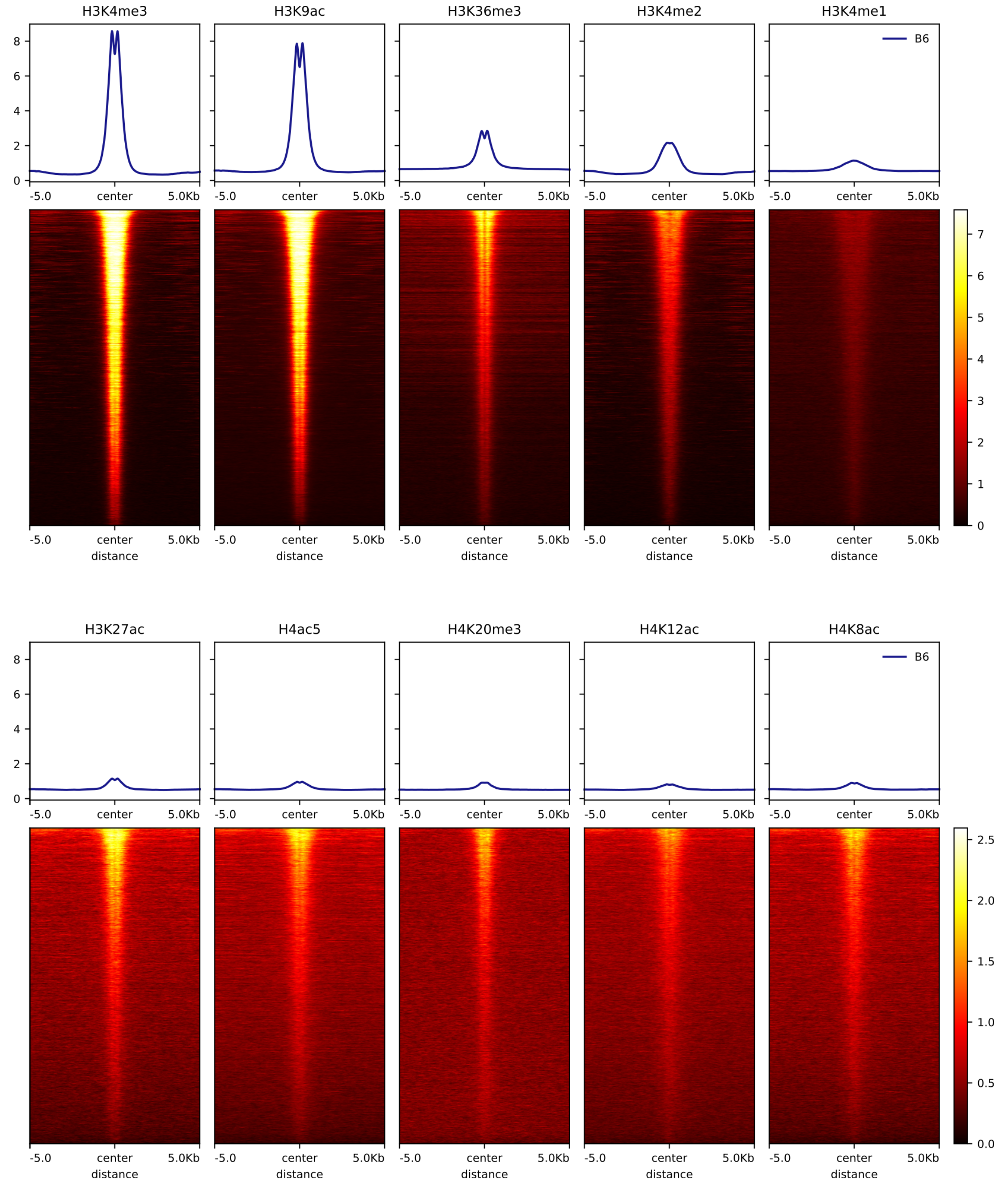
H3K4me3
H3K9ac
H3K36me3
H3K4me2
H3K4me1
B6
0
2
4
6
8
-5.0
center
5.0Kb
distance
0
1
2
3
4
5
6
7
H3K27ac
H4ac5
H4K20me3
H4K12ac
H4K8ac
B6
0.0
0.5
1.0
1.5
2.0
2.5

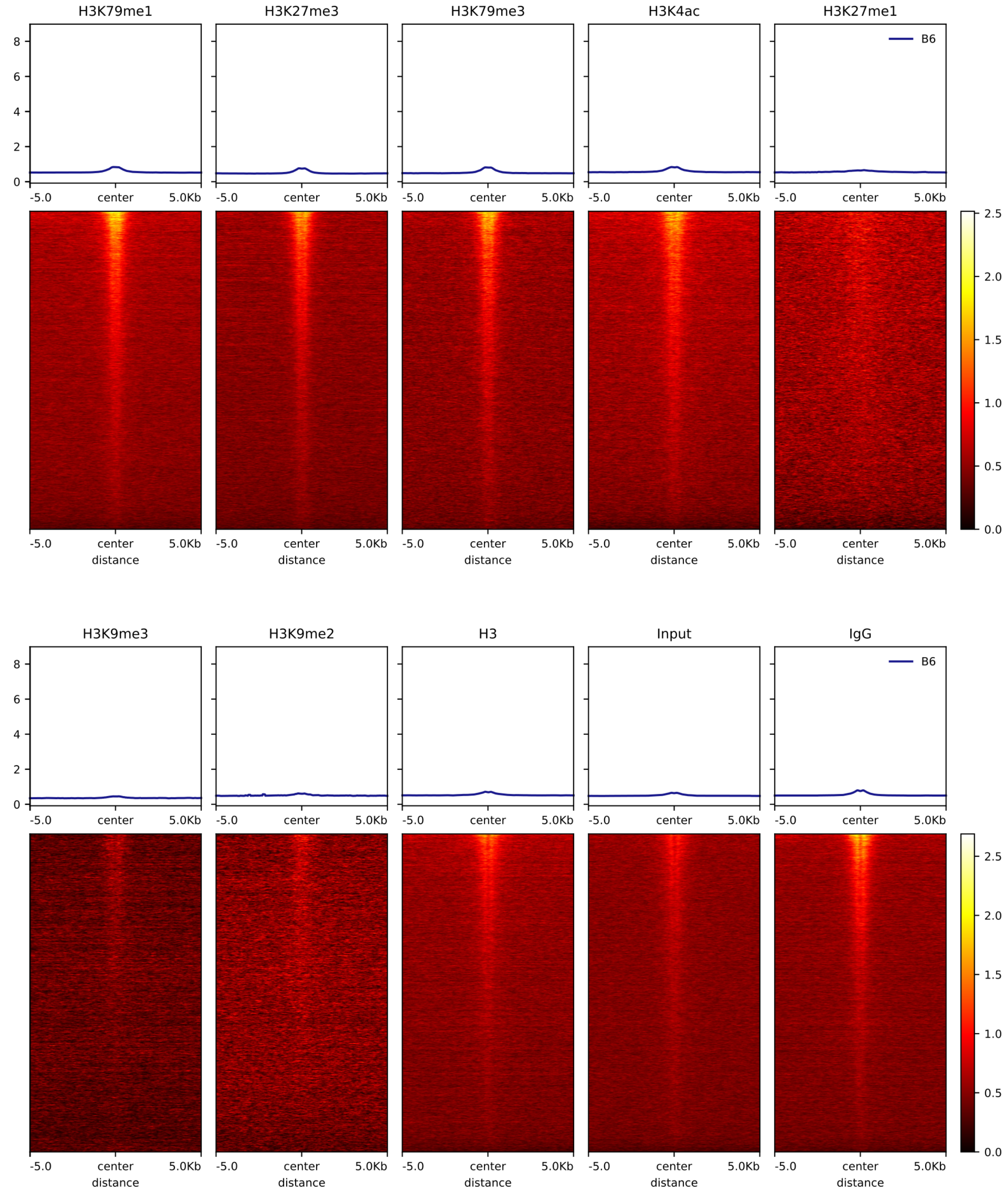

Supplementary Fig 5: Heatmaps of histone modification ChIP-Seq at DSB hotspots. Coverage data were averaged in 150bp windows and converted to reads per Kbp per million (RPKM) to facilitate cross-comparison. Heatmaps were generated using deeptools[53]. It is important to note that some enrichment at DSB hotspots is seen when using a non-specific antibody (IgG; last panel).

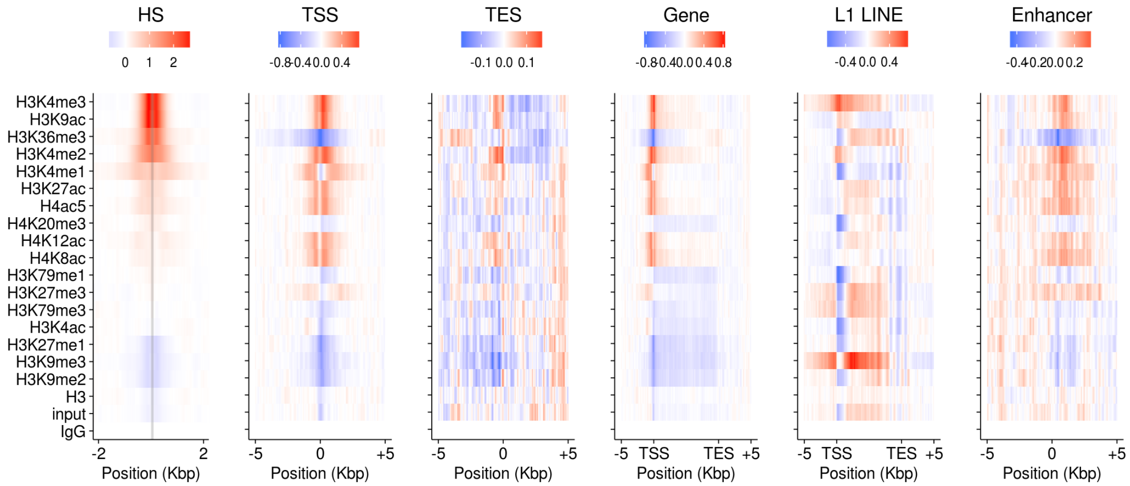

Supplementary Fig 6: Enrichment of histone modifications at functional genomic elements. Histone modification coverage was plotted around functional sites in the genome. Enrichment is shown as mean signal - mean signal in IgG ChIP-Seq (red=high; blue=low). L1 LINEs were obtained from the repeatmasker database. Enhancers were obtained from the UCSC table browser RefSeq functional elements table.

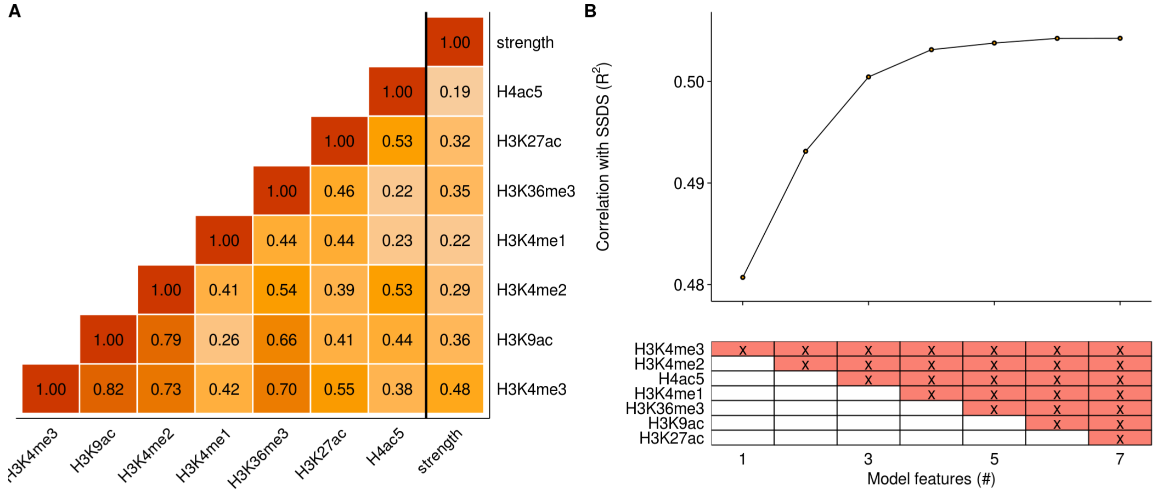

Supplementary Fig 7: Correlations between histone modifications and DSB hotspot strength. (A) Pearson correlation coefficients of log-transformed read counts and hotspot strength (strength). Only histone marks enriched at DSB hotspots were considered. Hotspots with above-zero coverage for all histone marks and hotspot strength were used (N = 11,253). (B) Multiple linear regression with histone marks only marginally improves correlation with DSB hotspots. The lower panel depicts the histone marks used (red; x) for models with each number of features. The order of addition was determined using all-subsets regression with the leaps package in R. Small increases in R^2 may simply arise because additional samples reduce stochastic noise in strength estimates.

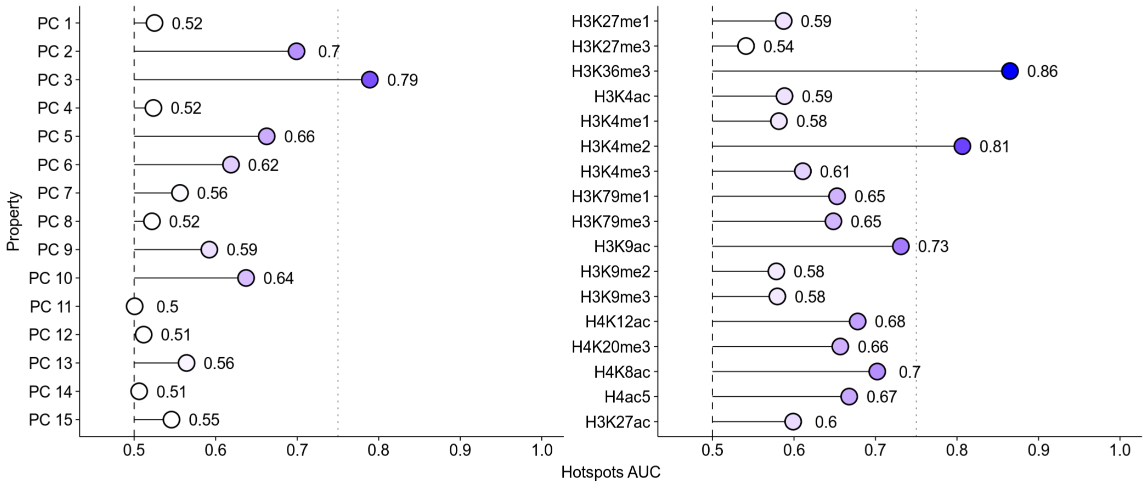

Supplementary Fig 8: Hotspots are distinguished from other H3K4me3 sites.

The area under the ROC curve (AUC) for discriminating hotspots from other H3K4me3 sites in the genome. AUCs for each principal component and for each histone modification are shown. Darker blue indicates higher AUC.